https://doi.org/10.1093/mnras/staf983

Echo mapping of the black hole accretion flow in NGC 7469

Raj Prince , 1,2,3* Juan V. Hernández Santisteban, Keith Horne, J. Gelbord, Ian McHardy, Ian McHardy, Ian McHardy, J. Gelbord, Ian McHardy, Ian McHardy, Ian McHardy, J. Gelbord, Ian McHardy, Ian McHardy, J. Gelbord, Ian McHardy, Ian McHard R. Edelson [®], ⁶ C. A. Onken [®], ⁷ F. R. Donnan [®], ⁸ M. Vestergaard [®], ^{9,10} S. Kaspi [®], ¹¹ H. Winkler [®], ¹² E. M. Cackett [®], ¹³ H. Landt, ¹⁴ A. J. Barth [®], ¹⁵ T. Treu [®], ¹⁶ S. Valenti [®], ¹⁷ P. Lira [®], ¹⁸ D. Chelouche [®], ^{19,20} E. Romero Colmenero , 21 M. R. Goad , 22 D. H. Gonzalez-Buitrago , 23 E. Kara 24 and C. Villforth

Affiliations are listed at the end of the paper

Accepted 2025 June 2. Received 2025 May 31; in original form 2024 May 18

ABSTRACT

Reverberation mapping (RM) can measure black hole accretion disc sizes and radial structure through observable light travel time lags that should increase with wavelength as $\tau \propto \lambda^{4/3}$ due to the disc's $T \propto r^{-3/4}$ temperature profile. Our 250-d RM campaign on NGC 7469 combines sub-day cadence 7-band photometry from the Las Cumbres Observatory robotic telescopes and weekly X-ray and UVOT data from Swift. By fitting these light curves, we measure the spectral energy distribution (SED) of the variable accretion disc, and inter-band lags of just 1.5 d across the UV to optical range. The disc SED is close to the expected $f_{\nu} \propto \nu^{1/3}$, and the lags are consistent with $\tau \propto \lambda^{4/3}$, but three times larger than expected. We consider several possible modifications to standard disc assumptions. First, for a $9 \times 10^6 \,\mathrm{M_\odot}$ black hole and two possible spins $a^* = (0, 1)$, we fit the X-ray-ultraviolet (UV)-optical SED with a compact relativistic corona at height $H_x \sim (46, 27) R_g$ irradiating a flat disc with accretion rate $\dot{m}_{\rm Edd} \sim (0.23, 0.24)$ inclined to the line of sight by $i < 20^{\circ}$. To fit the lags as well as the SED, this model requires a low spin $a^* \approx 0$ and boosts disc colour temperatures by a factor $f_{\text{col}} \approx 1.8$, which shifts reprocessed light to shorter wavelengths. Our Bowl model with $f_{col} = 1$ neglects relativity near the black hole, but fits the UV-optical lags and SEDs using a flat disc with $\dot{m}_{\rm Edd} < 0.06$ and a steep outer rim at $R_{\rm out}/c \sim 5-10$ d with H/R < 1 per cent. This rim occurs near the 10^3 K dust sublimation temperature in the disc atmosphere, supporting models that invoke dust opacity to thicken the disc and launch failed radiatively driven dusty outflows at the inner edge of the broad line region (BLR). Finally, the disc lags and SEDs exhibit a significant excess in the u and r bands, suggesting Balmer continuum and $H\alpha$ emission, respectively, from the BLR.

Key words: accretion, accretion discs – galaxies: active – galaxies: Seyfert – galaxies: individual: NGC 7469.

1 INTRODUCTION

The supermassive black holes (SMBHs) that lie at the centres of massive galaxies are crucial building blocks in the evolution and assembly of galaxies (Kormendy & Ho 2013; Combes 2023). The Event Horizon Telescope has produced spectacular images of the accretion flow very close to the SMBHs M87* and Sgr A* (Event Horizon Telescope Collaboration 2019, 2022). Despite these notable examples, the prospect of direct measurements of accretion disc for a large sample of SMBH across cosmic time remains out of reach. We currently rely on indirect measurements of rapidly accreting SMBH associated with active galactic nuclei (AGNs) to infer the mass of the black hole at its core and the size of the accretion disc that surrounds it. The most reliable technique to estimate these physical properties is known as reverberation mapping (Blandford & McKee 1982; Peterson 2014), which uses light travel time between different continuum bands and/or emission line variations as measurements of distinct regions within the AGN. This technique has successfully allowed measuring the sizes of the accretion disc, and broad-line

regions (BLR) and thus to infer SMBH masses for hundreds of AGNs (e.g. Peterson et al. 2004; Bentz & Katz 2015; Shen et al. 2024).

Intensive broad-band reverberation mapping (IBRM) campaigns with the Neil Gehrels Swift Observatory (Gehrels et al. 2004) and the global robotic telescope network of the Las Cumbres Observatory (LCO; Brown et al. 2013) play an essential role in monitoring dozens of AGNs at a high cadence (1-7 d) with broad-band photometry across a large energy range (e.g. McHardy et al. 2014, 2018; Shappee et al. 2014; Edelson et al. 2015, 2017, 2019; Fausnaugh et al. 2016; Troyer et al. 2016; Pal & Naik 2018; Cackett et al. 2020; Hernández Santisteban et al. 2020; Pahari et al. 2020). These IBRM campaigns are probing the smaller region of the accretion disc (and thus faster variability). In particular, these studies have established for the first time that AGN inter-band continuum lags increase smoothly with wavelength throughout the optical/ultraviolet (UV), consistent with the prediction of standard thin accretion disc theory (Collier et al. 1998; Cackett, Horne & Winkler 2007), and the discovery of excess lags especially around the Balmer jump, that are attributed to the diffuse continuum emission (DCE) from the BLR (Korista & Goad 2001, 2019; Netzer 2022). However, the disc sizes appear too large compared to the expected size from the standard accretion theory (Shakura & Sunyaev 1973) and there is no simple relation

Downloaded from https://academic.oup.com/mnras/article/541/1/642/8163832 by guest on 12 August 2025

^{*} E-mail: pr93@st-andrews.ac.uk, priraj@bhu.ac.in

between optical and X-ray variations. This strongly challenges the standard reprocessing model (Edelson et al. 2019) and stimulates the development of new models for the structure of the accretion flow and the origin of variability in AGN central engines (e.g. Gardner & Done 2017; Kammoun, Papadakis & Dovčiak 2019; Mahmoud & Done 2020; Sun et al. 2020).

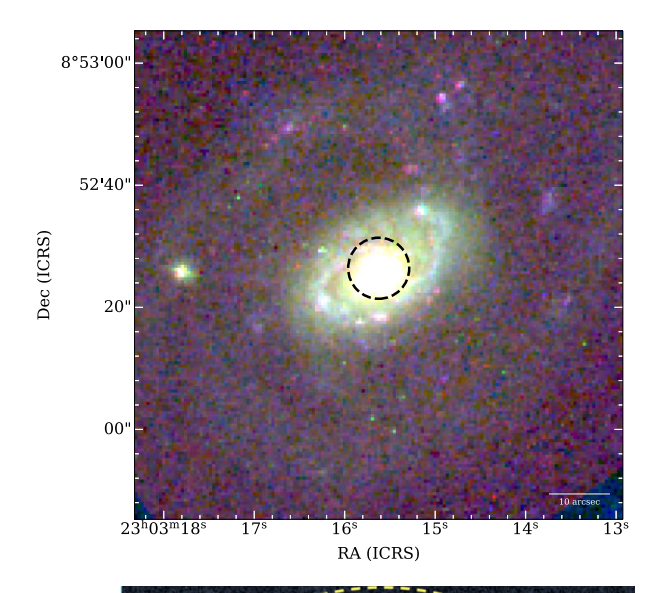
In this IBRM study, we revisit NGC 7469, a very bright (Seyfert 1943) and well-studied nearby (z = 0.016268; Springob et al. 2005) AGN with a 260-d campaign of intensive sub-day cadence monitoring with LCO and weekly monitoring with Swift. Already in the pioneering intensive monitoring experiment using International Ultraviolet Explorer (IUE) and Rossi X-ray Timing Explorer (RXTE), clear inter-band delays were measured between X-rays and the UV (Wanders et al. 1997; Collier et al. 1998; Nandra et al. 1998). In a recent re-analysis of those data, in combination with more recent Swift and ground-based monitoring, Pahari et al. 2020 derive crosscorrelation time lags relative to X-ray variations that constrain the size and radial temperature profile of the accretion disc. The lags increase with wavelength from ~ 1 d in the UV to ~ 3 d in the optical, with uncertainties of 0.5 to 1 d, a trend that is broadly consistent with the $\tau \propto \lambda^{4/3}$ relation expected for the $T \propto R^{-3/4}$ profile of an accretion disc. An opposite result is also observed in Kumari et al. (2023), where they found UV leading X-ray based on AstroSat data. These encouraging results from previous studies help to motivate our more intensive and longer-duration monitoring of NGC 7469 with LCO, which extends to longer wavelengths and significantly improves the lag constraints across the optical range.

The paper is structured as follows: Section 2 describes the observations and data reduction steps used to prepare the LCO and Swift data, including inter-telescope calibration of the LCO light curves. Section 3 details the time-series analysis, including inter-band lag measurements from the broad-band light curves, determination of the constant (host galaxy) and variable (AGN disc) SEDs. Interpretation of the results follows in Section 4, with modelling the SED to assess the energy budget, and to fit the lag spectrum to test models with a lamp-post geometry. In Section 5, we discuss possible scenarios to explain the larger-than-expected lag spectra, including DCE from the BLR, and reprocessing on a bowl-shaped accretion disc with a steep outer rim. We summarize our conclusions in Section 6. Throughout the work, we adopt the standard Planck cosmology with $H_0 = 69.6 \text{ km s}^{-1} \text{ Mpc}^{-1}$, $\Omega_M=0.286,$ and $\Omega_{\Lambda}=0.714,$ for which NGC 7469's redshift z = 0.016268 gives a luminosity distance $D_L = 71$ Mpc.

2 OBSERVATIONS

2.1 Las Cumbres Observatory

We monitored the multiwavelength flux variations of NGC 7469 nucleus in seven photometric bands (u, B, g, V, r, i, z_s) using LCO (Brown et al. 2013) 1-m robotic telescope network through a Key Project (PI: Hernández Santisteban). These telescopes are equipped with nearly identical Sinistro cameras covering a 26.5 \times 26.5 arcmin field of view with $4k \times 4k$ CCD detectors (0.389 arcsec pixel⁻¹). Our photometric monitoring spans 257 d, from 2021 May 11 through 2022 January 23, with 359 successful visits achieving a mean cadence of dt = 0.72 d. On each visit a pair of exposures was taken in each filter, providing an internal consistency check on statistical errors and a means of detecting outliers arising from cosmic ray hits or other issues. Exposure times were 120 s in u, 30 s in B, g, V, r, and i, and 60 s in z_s , typically achieving a photometric uncertainty of \sim 1 per cent, based on the light curves of comparison stars.



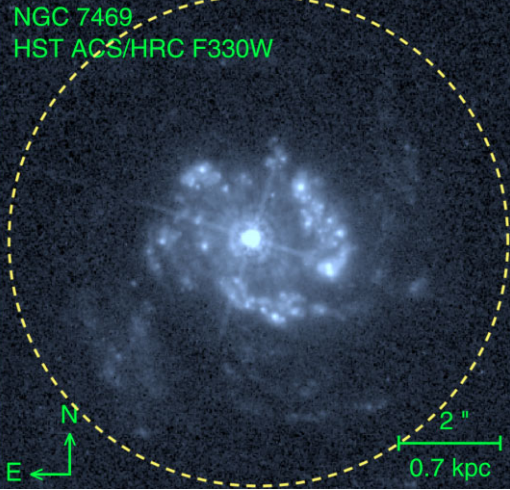


Figure 1. Top: combined *HST* image of NGC 7469 using archival data for the following filters: *F*660*N* (red), *F*547*M* (green), and *F*336*W* (blue). The LCO and *Swift* 5 arcsec radius aperture is shown as the dashed line. Bottom: *HST* image from Mehdipour et al. (2018) showing the starburst ring well inside the 5 arcsec radius aperture.

The processed CCD data downloaded from the LCO Archive¹ are bias and flat-field corrected images. The photometric extraction was performed through the AGN Variability Archive (AVA).² The details of the photometric extraction and absolute calibration can be found in Hernández Santisteban et al. (2020). We used SEXTRACTOR (Bertin & Arnouts 1996) to perform aperture photometry on the stars in the field. We use a 5 arcsec radius aperture, which provides a good compromise between signal-to-noise and seeing effects throughout the campaign. This aperture is shown in Fig. 1 in reference to a combined *Hubble Space Telescope (HST)* image of the host galaxy and its nuclear starburst ring. The aperture encloses significant host galaxy starlight, including the starburst ring. The starburst ring is studied in detail using Atacama Large Millimeter/submillimeter

¹http://archive.lco.global

²http://alymantara.com/ava

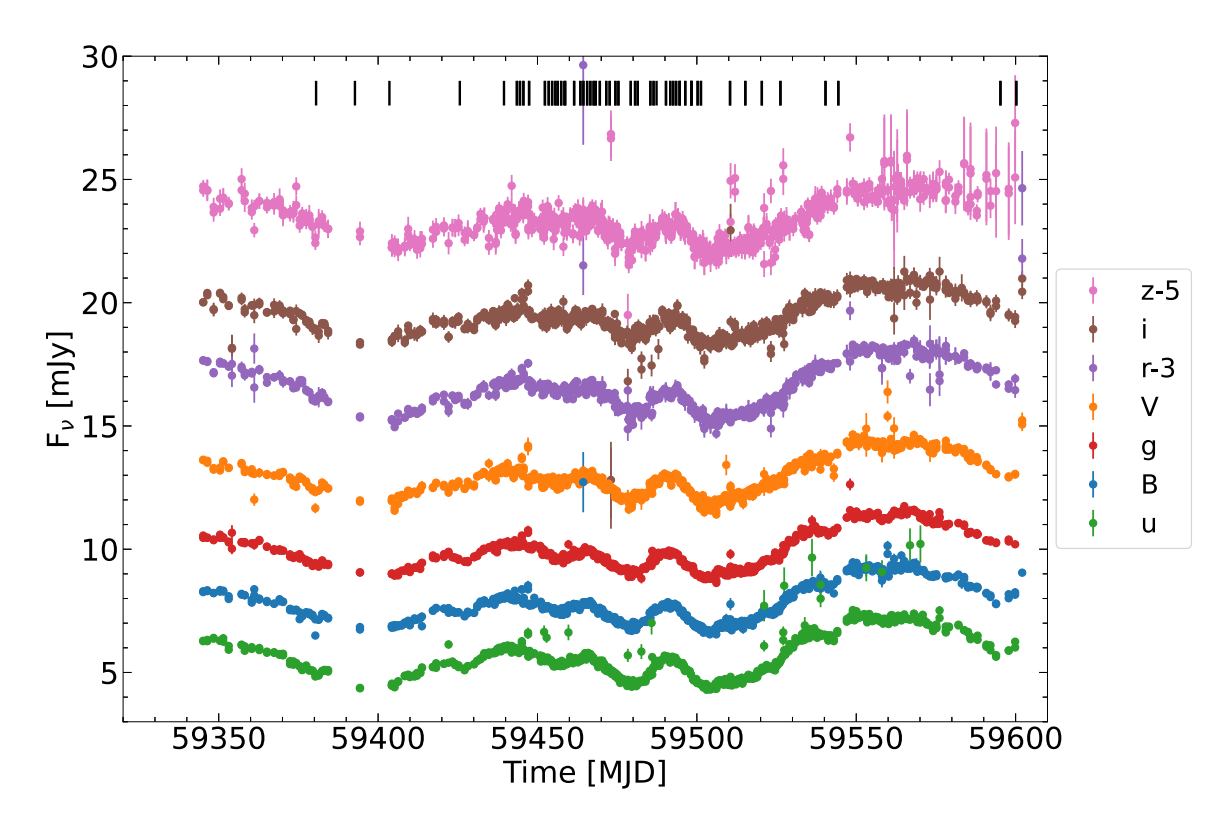


Figure 2. The inter-calibrated LCO light curves for NGC 7469 in seven broad-band filters (u, B, g, V, r, i, z_s) . The r and z_s light curves are shifted down by 5 mJy for clarity. The object is also monitored spectroscopically using a low-resolution spectrograph and the epochs at which FLOYDS spectra were taken are marked as black vertical lines along the top edge, but the FLOYDS data are not used in this work.

Array (ALMA) observation by Fathi et al. (2015), where they identify this region as an intense star-forming region.

We then obtain individual zero-points for each image by cross-matching the field with American Association of Variable Star Observers (AAVSO) Photometric All-Sky Survey (APASS) (Henden et al. 2018) and Panoramic Survey Telescope and Rapid Response System (PAN-Starrs; for z_s Flewelling et al. 2020) and performing a bootstrapping simulation to obtain the zero-point and its 1σ uncertainty. This correction was applied to all light curves before the inter-calibration described below.

2.1.1 Inter-telescope calibration

The LCO light curves are measured from CCD images obtained with nine 1-m robotic telescopes. While these telescopes and CCD cameras are nearly identical, slight differences in their CCD response, filter bandpasses, and observing conditions produce small additive and multiplicative offsets that we calibrate to align the light curve data from different telescopes (e.g. Hernández Santisteban et al. 2020; Donnan et al. 2023).

We used PYROA³ to inter-calibrate these light curves, as described in Donnan, Horne & Hernández Santisteban (2021) and Donnan et al. (2023). Briefly, PYROA models the light curve shape, X(t), as a running optimal average (ROA) of the inter-calibrated data from all the telescopes. The ROA model employs a Gaussian window function whose width Δ is one of the model parameters that is marginalized in the final calibration. Small Δ improves the likelihood but incurs a penalty for increasing the flexibility of X(t). Markov Chain

Monte Carlo (MCMC) methods based on the Bayesian Information Criterion (BIC) sample the joint posterior probability distribution over $3 \times 9 + 1 = 28$ inter-calibration parameters (additive offset B_i , multiplicative scaling A_i , and systematic uncertainty σ_i , for each of the nine telescopes, plus Δ). Default uniform priors are assumed and, because the LCO telescopes and detectors are nearly identical, constraints are applied to keep $\langle A_i \rangle = 1$ and $\langle B_i \rangle = 0$ averaged over all nine telescopes.

The inter-calibration model includes extra variance parameters σ_i , unique to each telescope, which are added in quadrature with the nominal error bars. Thus the telescopes that produce light curve data noisier than expected are penalized. Their weight is reduced when we define the light curve shape. Individual outliers on various epochs are also identified by expanding their error bars so that they deviate by no more than 4σ from the fitted model. This is a robust form of σ -clipping that reduces the need for human intervention to decide whether or not to omit specific outliers for subsequent analysis.

Fig. 2 presents the light curves and error bars that result from this inter-calibration procedure, showing that NGC 7469 exhibits a strongly correlated variability across the full optical range. The mean flux levels increase with wavelength and the variability amplitudes are approximately constant in F_{ν} . While inter-band time delays are not easily evident by eye, our subsequent analysis of these data defines inter-band time lags with a precision of order 0.1 d.

2.2 Swift Observatory

In parallel with our sub-day cadence LCO monitoring campaign, the Neil Gehrels *Swift* Observatory (*Swift* hereafter; Gehrels et al. 2004) was monitoring NGC 7469 with a weekly cadence as part of a long-term variability programme (PI: McHardy). We use the period

³https://github.com/FergusDonnan/PyROA

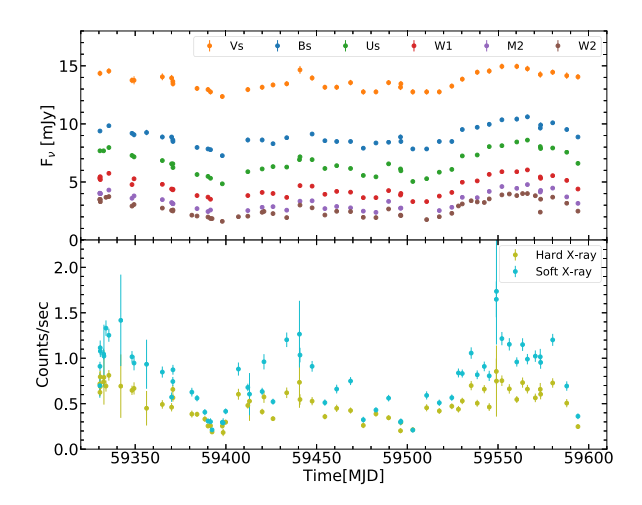


Figure 3. The *Swift* UVOT and XRT light curves, shown in the upper and lower panels, respectively, for periods overlapping with the LCO light curves in Fig. 2.

(MJD 59320–59600) that overlaps with the LCO monitoring period. Although the weekly cadence is insufficient to measure accurate time lags among the *Swift* light curves, we are able, by using the LCO light curves as a pattern, to estimate *Swift* lags relative to LCO with an accuracy of about 0.25 d. This helpfully extends useful lag measurements into the ultraviolet regime. The *Swift* data also afford a wider view of the spectral energy distribution (SED) including the optical, UV, and X-ray regimes. Accordingly, our analysis employs the ultraviolet and optical light curves from the Ultraviolet and Optical Telescope (UVOT; Roming et al. 2005) and X-ray data from the X-ray Telescope (XRT; Burrows et al. 2005) that were taken at times concurrent with our LCO monitoring. These *Swift* light curves are shown in Fig. 3.

The XRT observations were taken in photon counting (PC) mode, with an average exposure of ~ 1 ks. The light curve and spectral extraction were performed following the standard procedure described in Evans et al. (2009), via the web *Swift* XRT tools.⁴ The light curves were split into two broad-bands for their analysis: a soft X-ray band (0.3–2 keV) and a hard X-ray band (2–10 keV), as shown in the bottom panel of Fig. 3.

The UVOT light curves of NGC 7469, shown in the top panel of Fig. 3, were taken simultaneously with the X-ray observations, and make use of all six filters onboard Swift (3 UV bands – UVW1, UVM2, UVW2, and three optical bands – U, B, V). The light curves were extracted using a 5-arcsec radius aperture, and the exposure sensitivity maps were used to clip dropout measurements from the light curves (see details in Hernández Santisteban et al. 2020). Despite the lower cadence of these observations, they provide an anchor at shorter wavelengths to probe AGN variability extending into the UV and to retrieve the SED as shown in Section 4.

3 TIME-SERIES ANALYSIS

Our time-series analysis aims to measure for each band a mean flux, a variability amplitude, and a time delay. We do this using the PYROA code (see Donnan et al. 2021; Donnan et al. 2023, for details). PYROA models multiband light curve data assuming that all light curves have

the same shape X(t) but each light curve λ has a different background level $\bar{F}(\lambda)$, variation amplitude $\Delta F(\lambda)$, and time shift $\tau(\lambda)$:

$$F(\lambda, t) = \bar{F}(\lambda) + \Delta F(\lambda) X (t - \tau(\lambda)) . \tag{1}$$

The light curve shape X(t) is normalized to zero mean, $\langle X \rangle = 0$, and unit variance, $\langle X^2 \rangle = 1$, so that $\bar{F}(\lambda)$ is the mean and $\Delta F(\lambda)$ is the RMS of the model light curve at each wavelength. This is the model introduced in Donnan et al. (2021) to estimate time delays from the light curves of multiply lensed quasars.

The model in equation (1) approximates the delay distribution as a delta function, and thus neglects the temporal blurring caused by the range and distribution of delays that arise from the finite size and specific geometry of the reprocessing region. While this is clearly incorrect in detail, neglecting the width and shape of the delay distribution, it nevertheless provides useful lag measurements, especially when temporal blurring is not clearly detected in the light curves. The PYROA code can be used with finite width and different shapes for the delay distribution (Donnan et al. 2023), but we have not found it necessary to engage these additional parameters in our analysis.

3.1 PYROA fit to the 7-band LCO light curves

Our PYROA fit to the 7-band LCO light curve data is shown in Fig. 4. The parameters, summarized in Table 1, include for each band the mean flux \bar{F} , the RMS flux ΔF , the RMS of residual flux variations σ , and the time lag τ relative to the g band. The parameter uncertainties are derived from the MCMC samples. The ROA light curve shape X(t), for a Gaussian window function with an RMS of $\Delta=0.98$ d, is flexible enough to provide a good match to the data in all bands. Note that the uncertainty envelope (grey band) balloons out in two short data gaps, but otherwise, X(t) is tightly constrained. The ROA fit has also coped gracefully with the small fraction of outliers, for example, particularly in the u band in the top panel.

Normalized residuals plotted below each light curve indicate a generally successful fit. Slow trends remain in the residuals for some bands. For example, the model is below the data near the start for the r, i, and z_s bands, suggesting that slow flux variations with 0.1–0.3 mJy amplitudes may be present that are relatively red compared with the faster variations modelled by X(t) in equation (1). The PYROA model can be extended to fit these slow variations, but we have not pursued this here. The model light curve turns up rapidly at the end to fit a high flux in the final epoch. This feature is probably not real, but we have not removed this final epoch. It has little effect on the inferred lags.

Turning to the inter-band lags, the right column of panels shows posterior distributions from the MCMC samples of the lag parameters relative to the g band. Our fit includes two copies of the g-band data, one with and one without a lag parameter, to anchor the lags while providing a lag measurement and uncertainty for all bands, including g. The time lags are tightly constrained in all bands. They generally increase with wavelength but lags larger than this trend are found for the u and r bands. We attribute this to Balmer continuum emission in the u band and H α emission in the r band.

3.2 PYROA fit to 6-band Swift and 7-band LCO light curves

As Swift was monitoring NGC 7469 with weekly cadence during our intensive sub-day cadence LCO monitoring, we performed additional PYROA analyses fitting the Swift light curves on their own, with lags relative to UVW2, and fitting both Swift and LCO light curve data

⁴https://www.swift.ac.uk/user_objects/

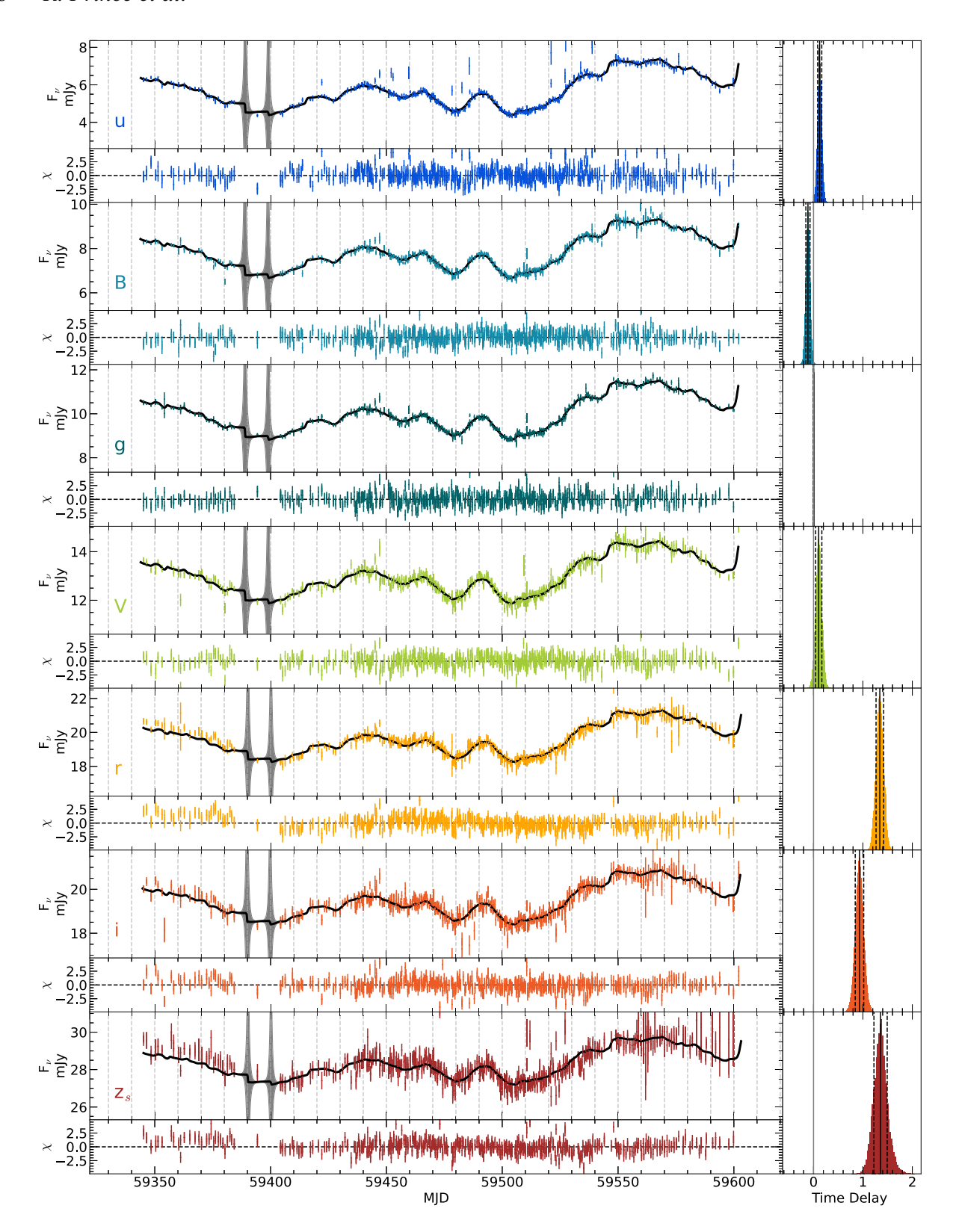


Figure 4. Simultaneous PYROA fit to LCO light curves in all seven photometric bands. Each light curve panel shows data (colour-coded error bars) and the best-fitting model light curve (solid black curve) with its 1σ uncertainty envelope (grey band). All fluxes are in mJy. The subpanel below each light curve shows the normalized residuals ($-5 < \chi < +5$) to the jointly fitted PYROA model. The right panel shows the marginalized posterior distribution for the time lag τ , relative to the g band light curve, with the median value and 68 per cent confidence interval indicated by vertical solid and dashed black lines, respectively. Time delays are in observed frame days. The parameters of this fit, including the mean and RMS fluxes and the lag measurements in each band, are summarized in Table 1.

Table 1. PYROA fit parameters for six *Swift* bands (W2, W1, Us, Bs, Vs) and seven LCO bands (Us, Us, Us,

			PYROA fit to the LCO+Swift light curves in Fig. 5			PYROA fit to LCO light curves in Fig. 4				
Filter	λ	$\Delta \lambda$	ΔF	$ar{F}$	τ	σ	ΔF	$ar{F}$	τ	σ
	(Å)	(Å)	(mJy)	(mJy)	(d)	(mJy)	(mJy)	(mJy)	(d)	(mJy)
Swift W2	1928	744	$0.673^{+0.009}_{-0.009}$	$2.697^{+0.010}_{-0.009}$	$-0.630^{+0.128}_{-0.136}$	$0.080^{+0.008}_{-0.007}$				
Swift M2	2246	530	$0.716^{+0.017}_{-0.016}$	$3.255^{+0.014}_{-0.015}$	$-0.420^{+0.196}_{-0.190}$	$0.081^{+0.015}_{-0.016}$				
Swift W1	2600	801	$0.773^{+0.013}_{-0.012}$	$4.495^{+0.012}_{-0.014}$	$-0.668^{+0.148}_{-0.154}$	$0.047^{+0.018}_{-0.022}$				
Swift Us	3465	662	$0.972^{+0.021}_{-0.019}$	$6.647^{+0.017}_{-0.016}$	$-0.469^{+0.202}_{-0.186}$	$0.098^{+0.021}_{-0.019}$				
LCO u	3508	638	$0.854^{+0.003}_{-0.003}$	$5.733^{+0.003}_{-0.003}$	$0.125^{+0.045}_{-0.045}$	$0.032^{+0.004}_{-0.004}$	$0.835^{+0.003}_{-0.003}$	$5.680^{+0.002}_{-0.002}$	$0.124^{+0.044}_{-0.044}$	$0.033^{+0.004}_{-0.005}$
LCO B	4361	951	$0.758^{+0.003}_{-0.003}$	$7.870^{+0.003}_{-0.003}$	$-0.124^{+0.044}_{-0.044}$	$0.006^{+0.006}_{-0.004}$	$0.741^{+0.003}_{-0.003}$	$7.823^{+0.002}_{-0.002}$	$-0.113^{+0.041}_{-0.041}$	$0.006^{+0.006}_{-0.004}$
Swift Bs	4392	866	$0.762^{+0.025}_{-0.025}$	$8.883^{+0.023}_{-0.023}$	$-0.958^{+0.325}_{-0.298}$	$0.125^{+0.032}_{-0.032}$				
LCO g	4770	1476	$0.766^{+0.002}_{-0.003}$	$10.031^{+0.002}_{-0.003}$	$0.003^{+0.038}_{-0.038}$	$0.005^{+0.005}_{-0.003}$	$0.749^{+0.002}_{-0.002}$	$9.983_{0.002}^{0.002}$	$-0.001^{+0.035}_{-0.037}$	$0.004^{+0.004}_{-0.003}$
Swift Vs	5468	655	$0.689^{+0.029}_{-0.029}$	$13.649^{+0.026}_{-0.026}$	$0.558^{+0.349}_{-0.412}$	$0.026^{+0.032}_{-0.018}$				
LCO V	5468	836	$0.730^{+0.004}_{-0.004}$	$13.028^{+0.004}_{-0.004}$	$0.102^{+0.061}_{-0.061}$	$0.054^{+0.006}_{-0.006}$	$0.713^{+0.004}_{-0.004}$	$12.982^{+0.004}_{-0.004}$	$0.105^{+0.063}_{-0.063}$	$0.053^{+0.007}_{-0.007}$
LCO r	6215	1400	$0.864^{+0.006}_{-0.006}$	$19.630^{+0.006}_{-0.006}$	$1.364^{+0.075}_{-0.083}$	$0.116^{+0.006}_{-0.006}$	$0.845^{+0.005}_{-0.005}$	$19.576^{+0.005}_{-0.005}$	$1.342^{+0.075}_{-0.078}$	$0.115^{+0.006}_{-0.006}$
LCO i	7545	1311	$0.704^{+0.006}_{-0.006}$	$19.516^{+0.006}_{-0.005}$	$0.942^{+0.086}_{-0.082}$	$0.084^{+0.009}_{-0.009}$	$0.689_{0.005}^{0.005}$	$19.472^{+0.006}_{-0.006}$	$0.930^{+0.087}_{-0.086}$	$0.082^{+0.009}_{-0.010}$
LCO z_s	8700	1024	$0.727^{+0.010}_{-0.010}$	$28.351^{+0.010}_{-0.009}$	$1.331^{+0.142}_{-0.136}$	$0.122^{+0.016}_{-0.020}$	$0.711^{+0.009}_{-0.009}$	$28.306^{+0.009}_{-0.009}$	$1.357^{+0.133}_{-0.134}$	$0.121^{+0.018}_{-0.023}$

sets together, with lags relative to the g band. Fig. 5 shows the results of the PYROA fit to all 13 light curves, with the data and model light curves in the left panels, and the corresponding lags in the right panels. Table 1 assembles the main parameters of this fit, including the mean and RMS fluxes, the rms residual parameter, and the lags relative to the g band light curve.

Including Swift data in this fit has almost no effect on the LCO lags or their uncertainties. Our fit to Swift data on their own did not define significant inter-band lags and this could be because of sparse sampling in the Swift data. However, the fit combining both data sets yields Swift lags relative to LCO g with uncertainties ranging from 0.14 d for W2 to 0.4 d for Vs. Two Swift bands, Bs and Vs, have response curves very similar to their LCO counterparts, B and V. Comparing their lags relative to g, the Swift Vs lag 0.56 ± 0.38 d is consistent with the more accurate LCO V lag 0.10 ± 0.06 d within 2σ , but the Swift Bs lag -0.96 ± 0.30 d is 2.8σ below the LCO B lag. The relatively large uncertainties in the Swift lags highlight the difficulty in measuring small lags with low-cadence monitoring data. The other issue with the Swift Bs and Vs bands is that they include a host galaxy contribution, which reduces the quality of data. Nevertheless, the Swift lags helpfully extend our optical LCO lag measurements to significantly shorter ultraviolet wavelengths.

We note that a somewhat longer lag occurs for the LCO u band relative to neighbouring bands at shorter and longer wavelengths. This feature is similar to the finding of excess u-band lags in most other well-studied AGNs (Fausnaugh et al. 2018; Hernández Santisteban et al. 2020) and is interpreted as due to Balmer continuum emission from the larger BLR mixing with the shorter lag from the accretion disc. Also noteworthy here is an apparent excess lag in the LCO r band, which has rarely if ever been reported in other AGNs. We attribute this to H α emission from the BLR.

3.3 X-ray to optical lag

We also used PYROA to measure a lag for the light curve of the full *Swift* X-ray band (0.3–10 keV) relative to the *g*-band light curve. We find a lag of $\tau_{\rm X-ray} = -1.8^{+1.2}_{-1.1}$ d. This low value is consistent with results from similar studies with joint *Swift* and LCO

reverberation mapping experiments (e.g. Edelson et al. 2019). We show this measurement in the lag spectrum of Fig. 8 and the lag spectrum fits in Section 4.2.

3.4 Flux-flux analysis and spectral energy distributions

Our flux-flux analysis, illustrated in Fig. 6, decomposes the observed light curves into constant (host galaxy) and variable (AGN disc) components, providing a separate SED for each component. The left panel of Fig. 6 uses our PYROA fit results to plot the observed fluxes, in mJy units, against the light curve shape $X(t-\tau)$, shifted in time to compensate for the time delay τ . Note that while the mean fluxes $\bar{F}_{\nu}(\lambda)$ increase with wavelength, the trend lines are nearly parallel, with slopes $dF_{\nu}/dX = \Delta F_{\nu}(\lambda)$ that are nearly the same at all wavelengths. The flux variations span a large range, up to a factor of ~ 2.5 between the brightest and faintest UVW2 fluxes during the campaign. The left panel of Fig. 6 shows also that these variations are linear, with no significant curvature that would be visible here if the AGN disc SED shape were to change as it brightens and fades. This validates the adequacy of our linear model, equation (1), which decomposes the observed variations into a constant component $\bar{F}_{\nu}(\lambda)$ and a variable component $\Delta F_{\nu}(\lambda) X(t-\tau)$.

From our PYROA model, the mean fluxes $\bar{F}_{\nu}(\lambda)$ occur at X=0, and the slopes $\Delta F_{\nu}(\lambda)$ give the rms amplitude of the variations at each wavelength. The faintest and brightest states observed in the monitoring campaign occur at $X_{\rm F}\approx-1.7$ and $X_{\rm B}\approx+1.9$, respectively. Anchored in the data between $X_{\rm F}$ and $X_{\rm B}$, the fitted linear trend line extrapolates to fainter levels, effectively turning down the light of the AGN disc. At $X_{\rm g}\approx-3.9$ the extrapolated UVW2 flux approaches zero, and the fluxes here define the SED of the host galaxy. By convention, we set $X_{\rm g}$ where the extrapolated UVW2 flux is 1 σ above 0. This is a lower limit because the host galaxy may have a more significant positive UVW2 flux from young high massive starts.

The right panel of Fig. 6 shows the resulting galaxy SED, $\bar{F}_{\nu} + X_g \Delta F_{\nu}$, and the AGN disc SED, $\bar{F}_{\nu} + (X - X_g) \Delta F_{\nu}$, at several brightness levels X, as well as their sum. The AGN disc SED is relatively blue, close to the expected $F_{\nu} \propto \nu^{1/3}$ power law, with

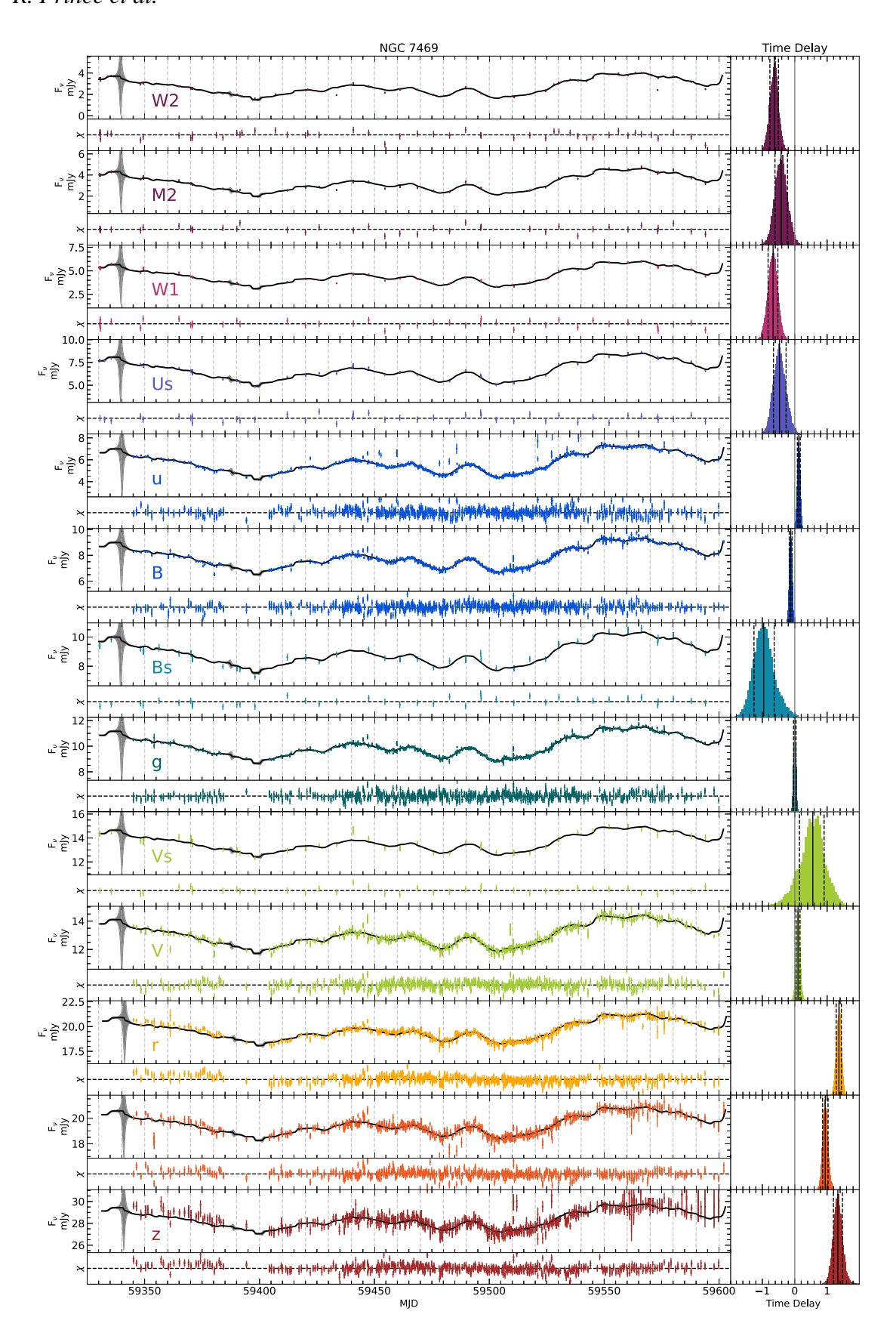
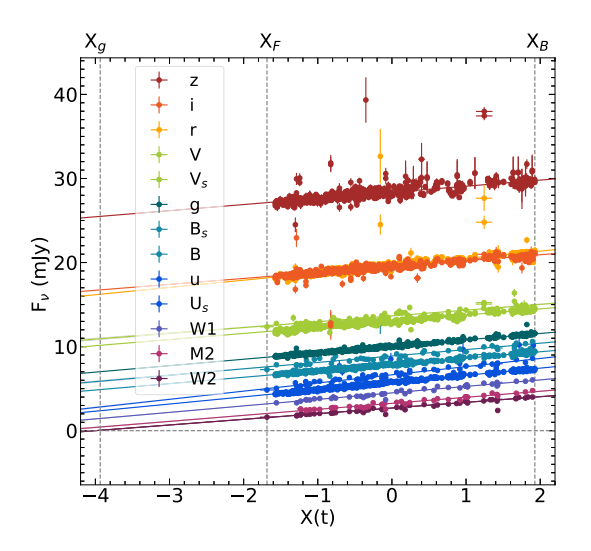


Figure 5. PYROA fits to all the 13 light curves, the weekly cadence *Swift* light curves in 3 UV bands (W2, W1) and 3 optical bands (Us, Bs, Vs) and the sub-day cadence 7-band LCO light curves (u, B, g, V, r, i, z, s). The panel format is the same as in Fig. 4.



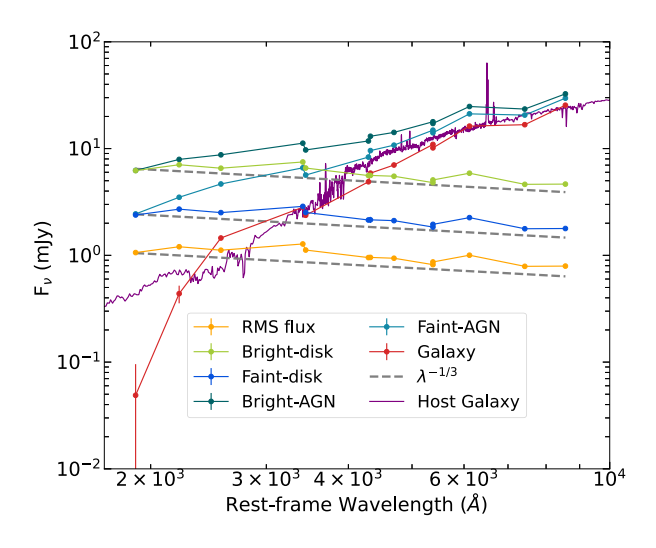


Figure 6. Results of the flux-flux analysis. The left panel shows the observed fluxes as a function of the dimensionless light curve shape X(t), which spans ± 1 for the mean \pm rms of the flux variations. The linear models fitted to the flux data adequately describe the variations in all bands, with the slopes dF_{ν}/dX giving the RMS of the light curve at each wavelength. Extrapolating to fainter levels, the W2 flux is 1σ above 0 at X_g . Evaluating the model fluxes at X_g gives the constant (host galaxy) SED. Subtracting this leaves the variable (AGN disc) SED, ranging from X_F at the faintest to X_B at the brightest during the campaign. The right panel shows the SEDs obtained from the flux-flux plot, corrected for Galactic dust extinction and reddening. The variable disc SEDs, faint, bright, and RMS, are close to the theoretical prediction, $F_{\nu} \propto \lambda^{-1/3}$, shown by the dashed grey lines. The host galaxy SED (red) is much redder. A possible host contribution of NGC 7469 type galaxy (NGC 5953) is plotted in purple which has a similar shape as the estimated one.

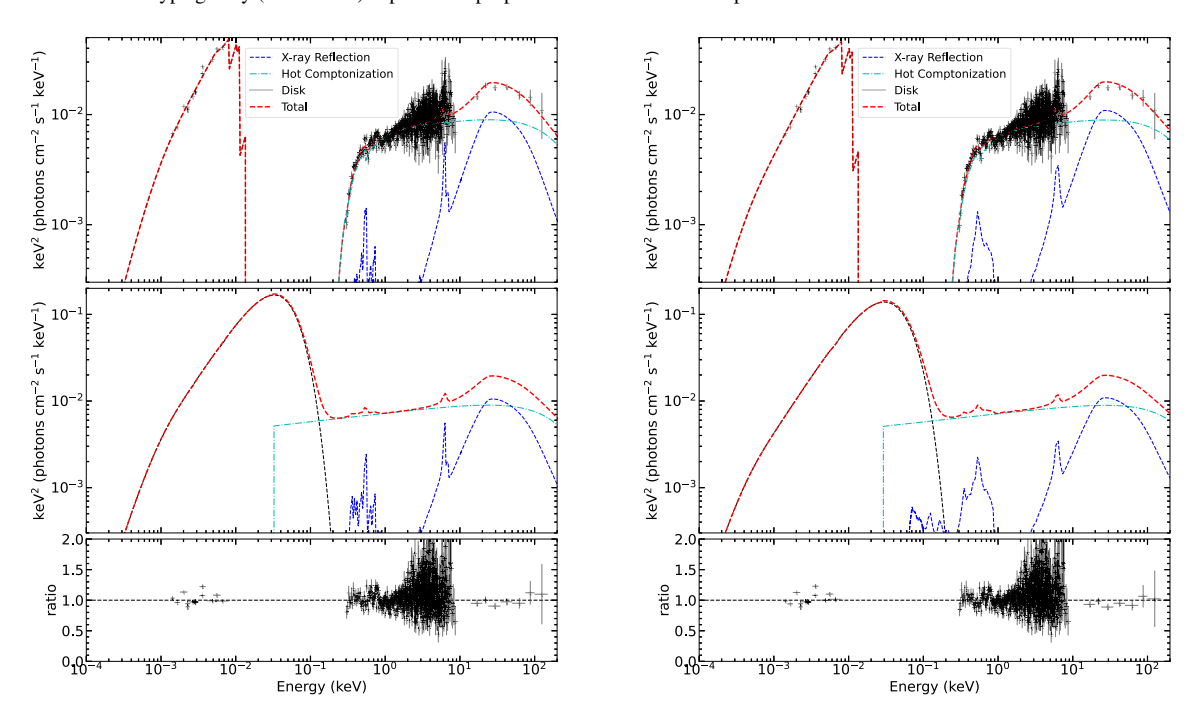


Figure 7. The broad-band averaged SED of NGC 7469 is fitted with the KYNSED model in XSPEC. The left panel shows the case when spin is fixed to a minimum value \sim 0 and the right panel represents the case when spin is fixed to a maximum value 1. The optical data points are the averaged disc emission from Table 2, the X-rays are from the *Swift* XRT between 0.3–10 keV and hard (15–200 keV) X-rays from the 70-month averaged *Swift* BAT spectra. The red dashed line on the top and middle panels represents the total model with and without galactic absorption. The middle panel shows the decomposition of the total model in the disc (black dashed line), hard-comptonization (cyan dot-dashed line), and reflection (blue dashed line) components. The lower panel shows the residuals of the fit. The best-fitting parameters are reported in Table 3.

departures at the 0.1 dex level. The relatively red host galaxy SED dominates in the optical spectrum and the AGN disc SED dominates in the UV. The galaxy SED and the faint and bright AGN disc SEDs, before and after correction for Galactic dust extinction, are tabulated in Table 2.

NGC 7469 has a circumnuclear starburst ring, with a radius of 1.8 arcsec (Díaz-Santos et al. 2007; Armus et al. 2023). As we see in Fig. 1, the starburst ring is well within our 5 arcsec radius aperture and we therefore expect UV emission from these hot young stars. This likely violates the convention of no significant

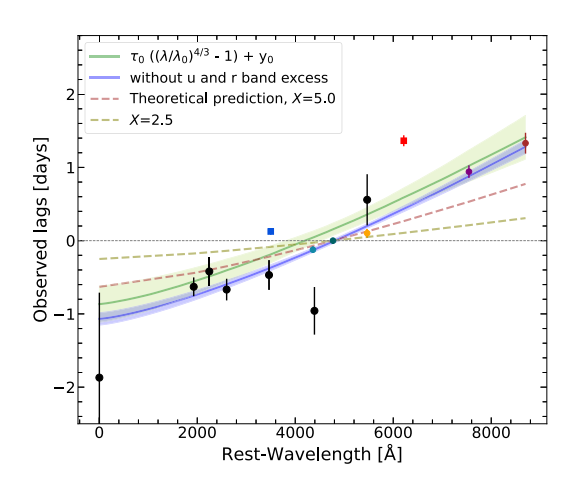


Figure 8. The lag spectrum $\tau(\lambda)$ derived from the measured time delays across the wavebands relative to the g band. The black data (solid circle) points are the *Swift* observations and the coloured ones are LCO's. The squares represent the u and r band excess. The time-lag data are fitted with $\tau = \tau_0 [(\lambda \lambda_0)^{4/3} - 1] + y_0$ and the error envelope is estimated from the best-fitting parameters and their uncertainties. The theoretical estimation considered the factors X = 2.5 and 5.0. The best-fitting parameters are mentioned in Table 4.

UV flux that we use to set X_g . We should therefore slide X_g to higher values, shifting a fraction of the AGN disc SED to the host galaxy SED. This makes the galaxy SED bluer, and scales the AGN disc SED down by a factor with little change in its spectral shape.

By modelling the HST image, we can estimate what fraction of the light within the 5 arcsec radius aperture arises from a point source versus the extended galaxy to obtain a better value of X_g . We have not pursued this analysis and we expect the ambiguity in X_g to have only a little effect on the interpretation of our results. However, we plot in Fig. 6 the spectrum of a galaxy with a mix of old and young stars, of similar type to NGC 7469. The shape is close but not a perfect match to the host galaxy SED derived from our flux–flux analysis, with a clear excess in the UVW2 band.

4 INTERPRETATION OF THE RESULTS

4.1 Fits to the spectral energy distribution

AGNs emit a very wide range of wavelengths and the complete information about the physical mechanism can only be accessed by modelling the broad-band emission. This also allows us to estimate the accretion rate and the total energy of the system. The broad energy range achieved by combining Swift and LCO light curves enables the study of the SED across the full X-ray, UV, and optical domains. To this end, we constructed the SED shown in Fig. 7. For the UV and optical SED, we use the average disc spectrum obtained from the flux-flux analysis (Table 2). For the X-ray SED, we collected all the XRT observations from the Swift archive for the period concurrent with our LCO monitoring (see Fig. 3) and constructed an average spectrum (covering the 0.3-10 keV range) using the online BUILD XRT PRODUCTS tool (Evans et al. 2009). To extend the SED to higher energies, we collected the 70 months of averaged spectra⁵ from Swift Burst Alert Telescope (BAT; Baumgartner et al. 2013) which cover the hard X-ray band (15-200 keV). This region is

particularly important as the corona's SED is expected to peak within this range (Haardt & Maraschi 1991).

We model with XSPEC12.13.1 (Arnaud 1996) the X-ray SED along with the average SED obtained from the flux-flux analysis, after subtracting the galaxy flux. We used the KYNSED model (Dovčiak et al. 2022) to fit the broad-band SED. Fig. 7 shows the best-fit achieved for two spin values, with the corresponding parameters and confidence intervals tabulated in Table 3. Fits performed for spin-zero $(a^{\star}=0)$ and maximally spinning $(a^{\star}=1)$ black holes are referred to as Model-1 and Model-2, respectively. As shown in Fig. 7 the KYNSED model consists of three components: the multitemperature blackbody emission from the accretion disc, the coronal emission (a power-law continuum with high-energy cut-off), and the X-ray reflection from the disc. The top and middle panels show the total and component SEDs with and without Galactic extinction, respectively, and the bottom panel shows normalized residuals.

KYNSED computes the emission from an accretion disc that is illuminated by the X-ray corona (point-like) located on the axis above the central black hole (lamp-post geometry). The output spectrum includes the thermal disc emission, primary X-ray emission as well as the X-ray reflection in a self-consistent way. More details about the model can be found in Dovčiak et al. (2022) and the model can be downloaded from the GitLab.⁶ It considers a Keplerian, geometrically thin and optically thick accretion disc with an accretion rate $\dot{m}_{\rm Edd}$, around an SMBH with a mass M_{\bullet} and spin a^{\star} . A colour correction, parametrized by f_{col} , alters the blackbody spectrum emitted by each annulus of the accretion disc, we keep it as a free parameter for both the cases and best-fitting values were recovered as shown in Table 3. The X-ray corona is modelled in the lamp-post geometry as a point source situated at height h above the black hole. The X-rays are emitted isotropically in the rest frame of the corona, with a power-law energy distribution parametrized by photon index Γ and high-energy exponential cut-off at $E_{\rm cut}$. The corona is powered by the accretion flow below a transfer radius r_{transfer} . Because the mechanism of transferring power from the inner accretion disc to the corona is not yet understood, the fraction of the accretion power transferred to the corona ($L_{\text{transfer}}/L_{\text{disc}}$) is fixed to 0.5.

The SED model parameters held fixed at typical values for this source include the redshift (z=0.016268), luminosity distance (71.0 Mpc), and black hole mass ($9\times10^6~{\rm M}_{\odot}$; Bentz & Katz 2015). We also fixed the parameters such as the accretion disc density ($10^{15}~{\rm cm}^{-3}$), and the Fe abundance (solar) (for details see Dovčiak et al. 2022). The remaining parameters are optimized for two cases of spin 0 and 1. The best-fitting parameters and 68 per cent confidence intervals listed in Table 3 are estimated using the MCMC package⁸ in XSPEC. Both spin 0 and 1 give a similarly good fit to the data, with $\chi^2/{\rm dof}=1169.2/526$ and 1194.8/526. While $\Delta\chi^2=25.6$ nominally favours $a^\star=0$, we report results for both cases.

For many of the SED parameters, the best-fitting values are similar for the two spin cases. The hydrogen column density ($N_{\rm H}$) accounts for absorption on the line of sight in our galaxy. Consistent values are found for $N_{\rm H}=(5.7,6.2)\times10^{20}~{\rm cm}^{-2}$ in both cases of spin. The accretion rate estimates, $\dot{m}_{\rm Edd}=23$ per cent for spin 0 and 24 per cent for spin 1, are similar and consistent within their uncertainties. The disc inclination is $i=14.9^{\circ}$ for spin 0 and 15° for spin 1, almost equal. The accretion disc outer radius is fixed at

⁵https://swift.gsfc.nasa.gov/results/bs70mon/

⁶https://projects.asu.cas.cz/dovciak/kynsed

⁷The accretion rate normalized to Eddington accretion rate. i.e. $\dot{m}_{\rm Edd} \equiv \dot{M}/\dot{M}_{\rm Edd}$, where \dot{M} is the accretion rate in physical units.

⁸https://heasarc.gsfc.nasa.gov/xanadu/xspec/manual/node43.html

Table 2. Results of the flux–flux analysis. We present the static component (associated with the galaxy) and the variable component in its faintest and brightest state (associated with the AGN), before and after Galactic extinction correction E(B-V)=0.069 (Schlegel, Finkbeiner & Davis 1998). These values are obtained from the joint analysis of the *Swift* and LCO data. The average AGN flux is estimated for X(t)=0 from the flux–flux plot shown in Fig. 6.

λ	Galaxy flux (Xg)	$AGN_{min}(X_F)$	$AGN_{max}(X_F)$	AGN _{min} (de-reddened)	AGN _{average} (de-reddened)	AGN _{max} (de-reddened)
(Å)	(mJy)	(mJy)	(mJy)	(mJy)	(mJy)	(mJy)
1928	0.049 ± 0.047	1.514 ± 0.055	3.946 ± 0.056	2.388 ± 0.086	4.178±0.080	6.223 ± 0.088
2246	0.438 ± 0.082	1.611 ± 0.094	4.198 ± 0.096	2.708 ± 0.158	4.737 ± 0.146	7.057 ± 0.161
2600	1.453 ± 0.065	1.739 ± 0.074	4.532 ± 0.076	2.513 ± 0.107	4.396 ± 0.099	6.550 ± 0.109
3465	2.822 ± 0.101	2.187 ± 0.116	5.699 ± 0.118	2.875 ± 0.152	5.029 ± 0.140	7.493 ± 0.155
3500	2.373 ± 0.015	1.921 ± 0.018	5.007 ± 0.018	2.522 ± 0.023	4.411 ± 0.021	6.573 ± 0.023
4361	4.887 ± 0.015	1.705 ± 0.018	4.444 ± 0.018	2.144 ± 0.022	3.750 ± 0.020	5.587 ± 0.023
4392	5.885 ± 0.124	1.714 ± 0.143	4.467 ± 0.146	2.151 ± 0.179	3.762 ± 0.166	5.606 ± 0.183
4770	7.017 ± 0.011	1.723 ± 0.014	4.491 ± 0.014	2.113 ± 0.017	3.696 ± 0.016	5.508 ± 0.017
5468	10.938 ± 0.143	1.550 ± 0.165	4.039 ± 0.168	1.841 ± 0.195	3.219 ± 0.181	4.798 ± 0.199
5468	10.156 ± 0.020	1.642 ± 0.023	4.280 ± 0.024	1.950 ± 0.028	3.411 ± 0.026	5.083 ± 0.028
6215	16.230 ± 0.030	1.944 ± 0.035	5.065 ± 0.036	2.256 ± 0.041	3.946 ± 0.038	5.880 ± 0.042
7545	16.746 ± 0.030	1.584 ± 0.035	4.127 ± 0.036	1.774 ± 0.039	3.104 ± 0.036	4.625 ± 0.040
8700	25.490 ± 0.051	1.636 ± 0.059	4.262 ± 0.060	1.784 ± 0.064	3.120 ± 0.059	4.649 ± 0.065

Table 3. SED parameters of the fitted KYNSED model for two values of black hole spin: Model-1 for spin, $a^{\star}=0$, and Model-2 for spin, $a^{\star}=1$. The best-fitting parameters and 68 per cent confidence intervals are estimated from the MCMC chain in XSPEC. Parameters held fixed include the redshift (z=0.016268), luminosity distance $(D_{\rm L}=71.0~{\rm Mpc})$, black hole mass $(M_{\bullet}=9\times10^6~{\rm M}_{\odot};{\rm Bentz}$ & Katz 2015), disc density $(10^{15}~{\rm cm}^{-3})$, and Fe abundance (solar) (see Dovčiak et al. 2022) and $L_{\rm transfer}=0.5$.

SED parameters	Units	Model-1 $a^* = 0$	$ \text{Model-2} \\ a^* = 1 $
Column density N _H	$10^{20}~{\rm cm}^{-2}$	$5.7^{+0.6}_{-0.3}$	$6.2^{+0.6}_{-0.6}$
Accretion rate $\dot{m}_{\rm Edd}$	per cent	23^{+1}_{-7}	24^{+2}_{-1}
$f_{ m col}$	-	1.82 ± 0.07	1.06 ± 0.10
Inclination i	deg	$14.9^{+1.6}_{-1.2}$	15.0^{+3}_{-2}
Outer radius r_{out}	R_g	10^{4}	10^{4}
Corona height h	R_g	46^{+4}_{-5}	27^{+10}_{-7}
Photon index Γ	_	$1.90^{+0.02}_{-0.03}$	$1.90^{+0.09}_{-0.02}$
High-energy cut-off $E_{\rm cut}$	keV	241^{+16}_{-6}	284^{+31}_{-48}
χ^2/dof .	-	1169.2/526	1194.8/526

 $r_{\rm out}=10^4\,R_g$ for both cases. The KYNSED model takes into account the height and luminosity of the hot corona. The corona height estimates are $h=46\,R_g$ for $a^\star=0$ and 27 R_g for $a^\star=1$, and the corona/disc luminosity ratio is fixed to 0.5. The coronal X-ray photon index $\Gamma=(1.90,1.90)$ and cut-off energy $E_{\rm cut}=(241,284)$ keV are consistent within the errorbar.

For the KYNSED model we used the XSET command in XSPEC to extract several additional physical parameters that are not directly reported in the model. For $a^{\star}=0$, the intrinsic and observed 2–10 keV X-ray luminosities are 0.065 and 0.058 in Eddington unit. The corona radius is $32~R_g$, the optical depth $\tau=0.99$ and the electron density in corona $n_{\rm e,c}=1.7\times10^{10}~{\rm cm^{-3}}$. Note this estimate for the coronal radius is comparable to its height. The innermost stable circular orbit (ISCO) radius and the inner edge of the disc are at 6 R_g . The transition (or transfer) radius is $\sim 31~R_g$ indicating that a significant accretion flow below this radius is transferred to the corona to heat the electrons. The ratio of transferred disc power to the corona is, $L_{\rm transfer}/L_{\rm disc}=0.5$. For spin 1, the ISCO radius and the

inner edge of the disc are at $1.4~R_g$. The transition radius at $\sim 6~R_g$ is much smaller than for $a^{\star}=0$ since a smaller inner part of the accretion disc suffices to power the corona. The power transferred to the corona from this part of the disc is $L_{\rm transfer}/L_{\rm disc}=0.5$. The corona radius is estimated as $14R_g$, the optical depth as 0.98, and the electron density in corona is $n_{\rm e,c}=3.85\times 10^{10}~{\rm cm}^{-3}$.

As suggested in Mehdipour et al. (2018), we also included the collisionally ionized component (cie) which is likely to be originated from the starburst activity in the source. The model has five parameters such as plasma temperature (which was kept free during the fitting), redshift, normalization, and abundance (fixed to solar), and the switch for the atomic data base. Two cases for the redshift were chosen once it was fixed to the nominal value 0.01626 and in the second case it was as a free parameter. To estimate the normalization we used the value provided in Mehdipour et al. (2018). In both cases, we do not see much improvement in the fit as the reduced χ^2 does not change much suggesting the starburst activity does not have much effect on our results.

To summarize, the KYNSED model tests a reverberation scenario in which the X-ray corona is powered by the inner disc, with the accretion-generated power that would normally be emitted as blackbody radiation from the inner disc transferred to and dissipated in the corona (Dovčiak et al. 2022). The corona then illuminates the accretion disc, elevating the disc temperatures and introducing reverberation and wavelength-dependent lags in the disc emission. An application of this model to the SED of NGC 5548, Dovčiak et al. (2022) find a corona height of 33–77 R_g and X-ray luminosity 45–70 per cent of the accretion disc luminosity. In our SED modelling of NGC 7469, we find a somewhat lower coronal height 27–46 R_{σ} and 50 per cent of the accretion power transferred to the corona. These findings indicate that the observed X-ray, UV, and optical SED can be generated by an accretion disc irradiated by an X-ray corona that is powered by the inner disc. Note, however, that a substantial fraction of the accretion power (not just a few per cent) must be transferred to the corona, and the corona height must be elevated to several tens of R_g above the black hole to explain the reprocessing. We now consider whether this scenario, with rapid changes in the inner region causing reverberations on the disc that move out at the speed of light, can also account for the observed inter-band lags.

652 R. Prince et al.

Table 4. Parameters of the power-law lag spectrum model (equation 2) fitted to the inter-band lag data as shown in Fig. 8. The 1σ uncertainties are scaled to make the reduced- $\chi^2 = 1$. We also show the *P*-value here and the *P*-value <0.05 suggests the fit does not explain the parameters well. A *P*-value <0.05 suggests that the fit explains the data well and the fit is acceptable.

Parameter	Units	LCO + Swift	Omit u and r
α		4/3	4/3
τ_0	d	1.02 ± 0.23	1.05 ± 0.08
<i>y</i> 0	d	0.15 ± 0.08	-0.01 ± 0.03
$\frac{\lambda_0}{\chi^2/\text{dof}}$	Å	4749	4919
χ^2/dof		221/(14-2) =	14.6/(12-2) =
		18.4	1.46
P-value		< 0.0001	0.1473

4.2 Disc size from the lag spectrum

A powerful diagnostic of the size and temperature profile of the accretion disc arises from the scaling of the time delays as a function of wavelength, known as the delay spectrum. We fit the measured lags given in Table 1 with a power-law model for the lag spectrum:

$$\tau(\lambda) = \tau_0 \left(\left(\frac{\lambda}{\lambda_0} \right)^{\alpha} - 1 \right) + y_0. \tag{2}$$

In this 3-parameter model, τ_0 is the light travel time delay corresponding to the disc size at the reference wavelength λ_0 . Within the accretion disc paradigm, α controls the shape of the disc radial temperature profile, $T \propto R^{-1/\alpha}$, and thus $\alpha = 4/3$ is expected for a thin steady-state blackbody accretion disc ($T \propto R^{-3/4}$; Shakura & Sunyaev 1973). We fix $\alpha = 4/3$ for the subsequent analysis. The parameter y_0 allows the model lag $\tau(\lambda_0)$ to depart from 0 since the best-fitting model need not pass exactly through the measured lag at λ_0 . We use a non-linear least-squares minimization procedure with LMFIT⁹ to fit this power-law model to the observed delay spectrum. The results are summarized in Table 4.

Our initial fit is shown as the green curve in Fig. 8. The seven *Swift* lags (black) have relatively large uncertainties compared with the seven LCO lags (in colour). The $\tau \propto \lambda^{4/3}$ model fits the LCO lags well apart from the u and r-band lags, which are significantly larger than the power-law model. The fit is formally rejected, with a reduced $\chi^2/\text{dof} = 221/(14-2) = 18.4$.

The *u*-band lag excess seen here is similar to what is often seen in the lag spectra of other well-studied AGNs (e.g. Cackett et al. 2018; Edelson et al. 2019; Hernández Santisteban et al. 2020) and is interpreted as a bias due to Balmer continuum emission in the *u* band. In addition to broad emission lines, the BLR emits a diffuse continuum that can respond to changes in irradiation. Given its larger size, the BLR responds with a larger lag than that of the more compact accretion disc (Korista & Goad 2001, 2019).

The r-band lag excess seen here is even more significant given its small uncertainty and is rarely noted in other AGNs. A possible hint of r-band lag excess can be seen in two other AGNs, MCG+08-11-011 and NGC 2617, but is not discussed in detail (see the lag spectra of Fausnaugh et al. 2018). A plausible origin for this excess lag is the strong and variable H α line emission in the r band.

With the u and r-band lag excesses having a physically motivated origin in the BLR response, we performed a second fit to the delay spectrum excluding the u and r lags. We retain the negative *Swift*

B-band lag, an outlier with no physically motivated explanation, but note that it has little effect given its uncertainty. With u and r on either side of the pivot wavelength, near the g band, the main change is in the y_0 parameter, shifting the model lags by 0.17 d. This second fit (blue curve in Fig. 8), is formally acceptable, with reduced $\chi^2/\text{dof} = 14.6/(12-2) \approx 1.46$. In both cases, the disc size at the reference wavelength is $\tau_0 \approx 1$ light d.

5 DISCUSSION

Having presented the main results of our intensive continuum reverberation mapping campaign on NGC 7469, we now interpret them by comparing them with accretion disc theory predictions for the SED and the delay spectrum.

5.1 Success and failure of standard accretion disc theory

We begin with a test of standard accretion disc theory by comparing the observed inter-band lags with theoretical predictions (Shakura & Sunyaev 1973; Cackett et al. 2007). A simple approach assumes that the accretion disc temperature profile $T \propto R^{-3/4}$ corresponds to a power-law lag spectrum $\tau = \tau_0 \ (\lambda/\lambda_0)^{4/3}$. This power-law model assumes a steady-state thin blackbody accretion disc, ignoring lower fluxes in the UV and infrared (IR) due to the finite temperature range between the inner and outer edges of the disc. Fig. 8 presents our fits of this power-law model to the measured lags, and the resulting values of $\tau_0 \approx 1$ d are detailed in Table 4.

To compare the disc size parameter, $\tau_0 \approx 1$ d, with the prediction of accretion disc theory, we use the following expression derived in Fausnaugh et al. (2016, see their equation 11 for details):

$$R_0 = \tau_0 c = \left(X \frac{k \lambda_0}{h c} \right)^{4/3} \left[\left(\frac{G M_{\bullet}}{8 \pi \sigma} \right) \left(\frac{L_{\text{Edd}}}{\eta c^2} \right) (3 + \kappa) \dot{m}_{\text{Edd}} \right]^{1/3}.$$
(3)

Here, $X \equiv h \, c/k \, T_0 \, \lambda_0$ is a dimensionless parameter that connects the reference wavelength λ_0 and temperature T_0 at radius $R_0 = c \, \tau_0$. $L_{\rm Edd}$ is the Eddington ratio, η is the disc's radiative efficiency, κ is the local ratio of external to internal heating assumed to be the same across all disc radii, and $\dot{m}_{\rm Edd}$ is the accretion rate in Eddington units. For the model lag spectra shown in Fig. 8, we adopt $\eta = 0.1$ and $\kappa = 1$, following Fausnaugh et al. (2018), and use the value of $\dot{m}_{\rm Edd} = 0.15$ (average of the spin 0 and 1 models) from Table 3.

One of the uncertainties in applying this model is the X factor in equation (3). The commonly adopted value of 2.5 corresponds to a flux-weighted radius at each wavelength (Guo, Barth & Wang 2022). However, a response-weighted radius is larger, perhaps as high as $X \sim 5$ (Fausnaugh et al. 2016; Tie & Kochanek 2017; Edelson et al. 2019). The predicted lag spectra for X = 2.5 and 5.0, corresponding to $\tau_0 = 0.33$ d and 0.83 d, are shown as the dashed lines in Fig. 8.

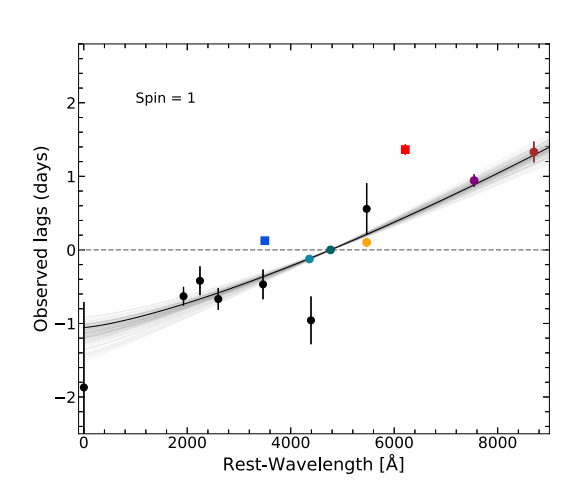
For X = 2.5 the observed lags exceed the predicted lags by a factor of 3, but for X = 5 the discrepancy is just 50 per cent.

5.2 Relativistic disc model with realistic X-ray reflection

Several possible modifications to the standard thin steady-state blackbody accretion disc reprocessing model have been considered to explain why the disc sizes inferred from continuum echo mapping are larger than expected (Kammoun et al. 2019; Jaiswal et al. 2023). Gaskell (2017) has also suggested that the observed larger lags could be the effect of reddening.

A means of testing the most sophisticated model currently available for continuum lag spectra is provided by Kammoun et al.

⁹https://lmfit.github.io/lmfit-py/index.html



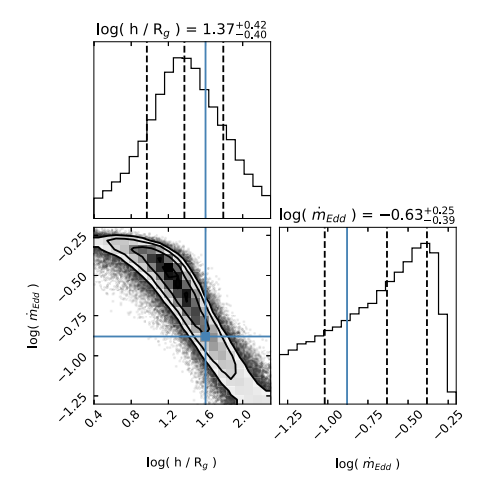


Figure 9. Left: the observed lag spectrum of NGC 7469 is modelled with the Kammoun et al. (2021, 2023) parametrization of lag predictions for an isotropic lamp-post irradiating a thin accretion disc, with realistic X-ray reflection and full treatment of relativity effects in the Kerr geometry of a 9 × 10⁶ M_☉ black hole with maximum spin $a^* = 1$. The best-fitting model (black solid line) and its 68 per cent uncertainty envelope (grey) are shown. The colours used for the lag data are the same as in Fig. 4. A horizontal dashed line $\tau = 0$ passes through the *g*-band lag at the reference wavelength (4770 Å). Right: the joint posterior distribution and the marginalized probability distributions for the two parameters of interest, the accretion rate \dot{m} in Eddington units, and the lamp-post height *h* in units of R_g . Vertical dashed lines mark the 16, 50, and 84 percentiles of the distributions, which are reported in Table. 5. This fit excludes the *u* and *r* lags, which are affected by Balmer continuum and Hα emission line respectively, and the colour temperature boost factor for the reprocessed emission from the disc is held fixed at $f_{col} = 2.4$. The best-fitting values of height and accretion rate from SED fit (Table 3) are marked in the right panel with blue (solid) colour.

(2021, 2023) in terms of a useful analytic parametrization of lag predictions for an isotropic lamp-post source irradiating a zerothickness accretion disc, with realistic X-ray reflection and full treatment of relativity effects in the Kerr geometry. In this model, the disc colour temperature is boosted above the effective temperature by a factor f_{col} , which increases lags by shifting the reprocessed light to shorter wavelengths. To apply this model to NGC 7469, we fix the black hole mass to $M_{\bullet} = 9 \times 10^6 \,\mathrm{M}_{\odot}$ (Bentz & Katz 2015). The analytic model requires an estimate for the 2-10 keV X-ray luminosity. For this we adopt $L_X = 1.45 \times 10^{43} \text{ erg s}^{-1}$, as derived from our broad-band SED model, corresponding to $L_{X,Edd} = 0.012$ in Eddington units. We consider two cases of spin: $a^* = 0$ for a Schwarzshild black hole, and $a^* = 1$ for a maximally spinning Kerr black hole. The predicted lags then depend mainly on three parameters: the accretion rate (\dot{m}) , the lamp-post height (h), and the colour temperature factor (f_{col}). For a viable model, the constraints on h and \dot{m} from the lag data should overlap with those given in Table 3 from the SED fit in Fig. 7.

We performed fits to the inter-band lag data both including and excluding the u and r lags, which may be affected by Balmer continuum and H α emission. We consider initially two fixed values $f_{col} = 1.5$ and 2.4 and employ the PYTHON package EMCEE (Foreman-Mackey et al. 2013) to explore the (h, \dot{m}) parameter space, with uniform priors, and 32 MCMC walkers taking 5×10^4 steps. Fig. 9 shows our fit to the lag data, excluding the u and r lags, for spin 1, and for $f_{\rm col}=2.4$. This model provides a good fit for the lag data. The model predicts a lag spectrum close to $\tau \propto \lambda^{4/3}$ since reprocessing occurs on the flat disc with $T \propto r^{-3/4}$ in regions far enough from the black hole that relativity effects can be neglected. Similarly good fits to the lag data are achieved for all cases we considered but with different values of h and \dot{m} . The case shown in Fig. 9 has the best match between constraints from fitting the lags and those from fitting the SED. Note the strong anticorrelation between h and \dot{m} , which can be understood since increasing h allows each disc annulus to intercept a larger solid angle of the lamp-post irradiation, and thus the accretion rate can be reduced to maintain the same effective temperature.

Table 5. Constraints on the lamp-post height h and accretion rate \dot{m} derived by fitting the inter-band lag data with Kammoun's analytic expression for fixed values of the colour correction $f_{\rm col} = (1.5, 2.4)$, black hole spin $a^* = (0, 1)$, and for fits including and excluding the u and r lags.

Parameters	$f_{\rm col}$:	= 2.4	$f_{\rm col} = 1.5$		
-	$a^* = 0$	$a^{\star} = 1$	$a^{\star} = 0$	$a^{\star} = 1$	
$\log (h/R_g)$	$0.90^{+0.32}_{-0.31}$	$0.99^{+0.30}_{-0.33}$	$1.05^{+0.38}_{-0.38}$	$1.93^{+0.32}_{-0.20}$	
$\log{(\dot{m}_{\rm Edd})}$	$-1.19_{-0.06}^{+0.07}$	$-0.45^{+0.11}_{-0.21}$	$-0.36^{+0.04}_{-0.08}$	$-0.21^{+0.02}_{-0.05}$	
	excluding	u and r band			
$\log (h/R_g)$	$1.17^{+0.32}_{-0.41}$	$1.37^{+0.41}_{-0.40}$	$1.63^{+0.30}_{-0.45}$	$2.09^{+0.17}_{-0.27}$	
$\log{(\dot{m}_{\rm Edd})}$	$-1.23^{+0.07}_{-0.05}$	$-0.63^{+0.25}_{-0.38}$	$-0.49^{+0.11}_{-0.22}$	$-0.25^{+0.04}_{-0.06}$	

Note. ¹ Analytical expression is provided in Kammoun et al. (2021, 2023).

Table 5 summarizes, for each of the eight cases considered, the best-fitting parameters (h, \dot{m}) . Fig. 10 plots these results to show that the relatively tight constraints from the SED fit overlap with those from the lag fit for $f_{\rm col}=2.4$. For $f_{\rm col}=1.5$, and for lower values, the accretion rate required to fit the lags is well above that found in the SED fit, and can thus be ruled out.

For $f_{\rm col}=2.4$, the accretion rate from the lags is lower than that from the SED for spin 0, and vice versa for spin 1. An intermediate spin may thus provide an accretion rate consistent between the lag and SED data. However, for both spins the lag fit for $f_{\rm col}=2.4$ gives $h\sim 10~R_{\rm g}$, smaller by a factor of 2 to 4 than that required by the SED. The uncertainties from the lag fit are large enough that this discrepancy is only marginally significant. When we omit the u and r lags the required height increases by about a factor 2, improving the consistency between the lag and SED constraints. We conclude provisionally that a model with $f_{\rm col}\sim 2.4$ can probably fit both the SED and the lag constraints.

A detailed parameter exploration is done in Kammoun et al. (2023) for various reverberation-mapped AGNs. They find and discuss a range of parameter degeneracies arising from fits to the lag spectra.

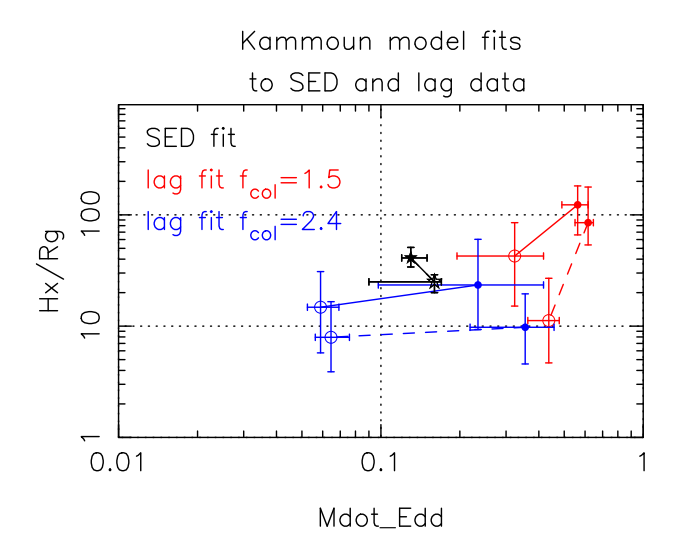


Figure 10. Constraints on the lamp-post height H_x and accretion rate $m_{\rm Edd}$ in Eddington units for the Kammoun et al. (2021, 2023) model, which features a compact isotropic lamp post model of the X-ray corona, fully relativistic light propagation near the black hole, and realistic treatment of the X-ray reflection from the disc. Open and filled symbols are for spin 0 and 1, respectively. Black solid stars mark the tight constraints from the SED (Table 3, Fig. 7). Circles mark constraints from fits to the inter-band lags (Table 5) for $f_{\rm col} = 1.5$ (red) and 2.4 (blue). Lines connecting spin 0 and spin 1 constraints are dashed for lag fits that include the u and r bands. The SED and lag constraints overlap for $f_{\rm col} \sim 2.4$.

In particular, $f_{\rm col} > 1$ is always needed to fit the lag data, but with different corona heights, accretion rates, and black hole spin in each AGN. The corona height and accretion rate estimated for NGC 7469 in our work are in the range provided for various objects in Kammoun et al. (2023).

To investigate the constraints in more detail, Fig. 11 summarizes for both spins 0 and 1, and for a range of $f_{\rm col}$, the constraints on the accretion rate \dot{m} , lamp height h, and inclination i arising from the fitting of the lag data compared to those of the fitting of the SED data. To create this plot, we first ran a series of fits to the SED data to obtain for a grid of fixed values of $f_{\rm col}$, best-fitting parameters and uncertainties for \dot{m} , h, and i (black points with error bars in the lower three panels). The top panel identifies best-fitting values of $f_{\rm col}$, 1.84 ± 0.06 for spin 0 and 1.07 ± 0.07 for spin 1, that minimize the χ^2 and maximize the relative probability $P_{\rm rel} \propto \exp\left(-\Delta\chi^2/2\right)$. A similar series of fits to the lag data then yields the red points with error bars in the lower three panels. For a consistent model, the lag constraints (red) and SED constraints (black) should agree.

The best-fitting inclination is small $i < 20^\circ$ for both spins. The SED data fairly tightly constrain the accretion rate, $\dot{m} \approx 0.25$ in Eddington units, with little dependence on $f_{\rm col}$ or spin. The lag data, however, admit a strong degeneracy of the form $\dot{m} \propto f_{\rm col}^{-4}$, which arises from the disc temperature profile $T_{\rm eff} = (T/f_{\rm col}) \propto \dot{m}^{1/4} R^{-3/4}$. In Fig. 11, we show two lag fits, one (in red) with h optimized for each $f_{\rm col}$, and another (in blue) with h fixed at the best-fitting value from the SED fit. Note that the spin 0 model can fit both the SED and the lags with a consistent $\dot{m} \approx 0.25$, but with a high $f_{\rm col} \approx 1.8$, and with somewhat discrepant lamp heights, $h \sim 50$ for the SED fit and $h \sim 10$ for the lag fit a 2σ discrepancy given the 0.4 dex uncertainty in h from the lag fit. With $h = 46~R_g$ to match the SED fit, the lag fit (blue) reduces \dot{m} by a factor of 2, again 2σ below the SED fit. For spin 1 the SED fit again finds $\dot{m} \approx 0.25$ with a very plausible $f_{\rm col} = 1.1$. Unfortunately, this combination fails to fit

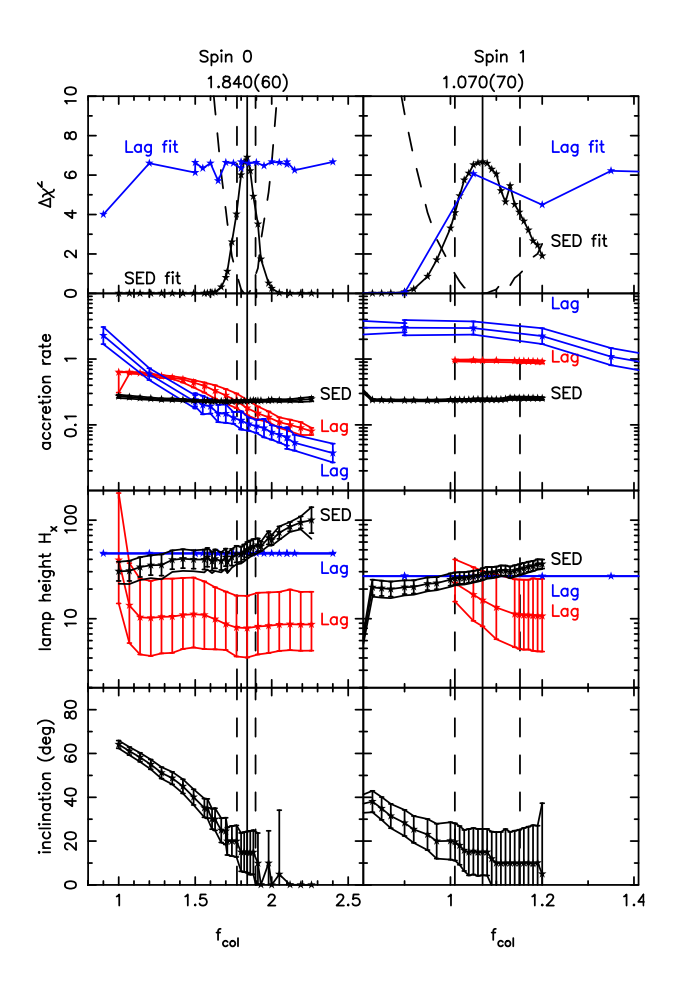


Figure 11. Results of fitting the SED and lag spectra for spin 0 (left column) and spin 1 (right column). Three cases shown are the SED fit (black), and lag fits with lamp height free (red) and fixed (blue). The results shown are for grids of fixed values of the disc colour temperature $f_{\rm col}$. Top row shows $\Delta\chi^2$ for the SED fit (dashed parabola) and relative probabilities $P_{\rm rel} \propto \exp\left(-\Delta\chi^2/2\right)$ for the SED fit (black) and for the lag fit (blue). The second row shows constraints on the accretion rate \dot{m} in Eddington units. The third row shows constraints on the lamp height H_x in units of R_g . The bottom row shows constraints on the disc inclination. The SED data provide tighter constraints than the lag data. The best-fitting $f_{\rm col}$ and its uncertainty based on $\Delta\chi^2=1$ are indicated at the top and by vertical lines. The lag data provide a degenerate constraint of the form $\dot{m} \propto f_{\rm col}^{-4}$, arising from the disc temperature profile $T_{\rm eff}=(T/f_{\rm col}) \propto \dot{m}^{1/4}\,R^{-3/4}$.

the lags, which require $\dot{m}\sim 0.25~(1.8/f_{\rm col})^4$, an order of magnitude higher than from the SED fit. The χ^2 favours the spin 0 model, but the required boosting of disc temperatures by a factor of 1.8 is quite high. However, some of the earlier studies modelling the extreme ultraviolet (EUV) and soft X-ray emission from AGN have used $f_{\rm col}=2.4$ (Done et al. 2012) and also for X-ray binaries it has been shown that the $f_{\rm col}$ can be around 1.7 (Shimura & Takahara 1995; Mirzaev et al. 2024).

Note that $f_{\rm col} \sim 1.8$ implies that the colour temperature of the reprocessed emission from the outer disc is boosted considerably above the effective temperature. This shifts the reprocessed emission to shorter wavelengths and thus increases the lags at a given wavelength. The physical motivation for introducing $f_{\rm col} > 1$ is to approximately describe the effect of electron scattering in the disc atmosphere (Kubota & Done 2018). This is appropriate for the hotter regions of the disc $(T > 10^5 \, {\rm K})$ where electron scattering

dominates the opacity, but not for the cooler disc regions ($T < 10^4 \, \mathrm{K}$) where $f_{\mathrm{col}} = 1$ should apply. For these flat-disc models, blackbody reprocessing ($f_{\mathrm{col}} = 1$) fails to fit the lags, and the finding that $f_{\mathrm{col}} \sim 1.8$ is needed to fit the lags is another way of quantifying the problem of disc sizes being larger, and thus hotter at each radius, than expected.

5.3 Bowl model with power-law disc thickness profile

Another option that may help to explain why disc sizes inferred from continuum reverberation mapping are larger than expected is to retain blackbody reprocessing with $f_{col} = 1$ but relax the assumption of a flat disc thickness profile H(R). Starkey et al. (2023) investigate how vertical structure on the disc surface affects the lag spectrum. They find that steeply sloped rims or wave-like ripples can have the desired effect of increasing the lags. The inwardly tilted slopes intercept more flux from the central lamp-post than a flat disc surface. This elevates the local temperature and thus shifts the lagged blackbody response to shorter wavelengths. Applied to the 2014 Space Telescope and Optical Reverberation Mapping (STORM) campaign data on NGC 5548, these models succeed in fitting the larger-than-expected lags simultaneously with the faint and bright disc SEDs. In particular, an increase in disc thickness (Baskin & Laor 2018), or launching of a failed radiatively accelerated dusty wind at the inner edge of the BLR (Czerny & Hryniewicz 2011) is expected at the radius where the disc temperature profile crosses the dust sublimation threshold at ~ 1500 K. This promising model works for NGC 5548 and, given the connection with upward radiation pressure on dust in the disc atmosphere, it may apply more generally to all AGN discs.

We now apply to NGC 7469 this blackbody reprocessing model on a disc with a concave power law H(R) thickness profile. We refer to this as the Bowl model, since the concave H(R) profile can resemble the interior surface of a bowl. A pair of lamp-posts, isotropic point sources with bolometric luminosity L_x located at $\pm H_x$ above and below the central black hole, irradiate the disc surface at radius R and height $\pm H(R)$ above and below the disc plane. Balancing heating and radiative cooling, the effective temperature T(R) is given by

$$\sigma T^{4}(R) = \frac{3 G M_{\bullet} \dot{M}}{8 \pi R^{3}} \left(1 - \left(\frac{R_{\text{in}}}{R} \right)^{1/2} \right) + \frac{L_{x} (1 - A) \cos \theta}{4 \pi \left(R^{2} + (H(R) - H_{x})^{2} \right)}, \tag{4}$$

Here, G is Newton's gravitational constant, σ is the Stefan-Boltzmann constant, and M_{\bullet} is the black hole mass. The first term represents heating by the viscous dissipation and torques associated with the accretion rate \dot{M} . For zero torque between the disc and the black hole, the viscous heating vanishes at the inner radius $R_{\rm in}$, which we assume is at the ISCO. The second term accounts for irradiative heating from the lamp-posts. The disc albedo A is assumed to be independent of R. For a thin disc the grazing incidence angle θ is close to 90°. For a thin flat disc, $\cos\theta\approx(H_x-H)/R$ so that both terms scale as R^{-3} at large R. This introduces a degeneracy between accretion power and irradiation, i.e. between M_{\bullet} \dot{M} and $L_x(H_x-H)(1-A)$.

The Bowl model as currently implemented makes simplifying assumptions such as isotropic point source lamps, radius-independent disc albedo, blackbody reprocessing, and Euclidean geometry neglecting relativity effects (Doppler boost, gravitational redshift, light trajectory bending). A more detailed modelling of the inner disc region would be needed to enable the Bowl model to fit the observable X-ray spectrum, and predict the unobservable EUV spectrum, but

this is beyond the scope of this paper. As a consequence, parameters associated with the region near the black hole are unreliable and should be regarded as a useful approximate description of the irradiation that emerges to reach the outer disc at $R\gg R_g=G\,M_\bullet/c^2$ where neglecting relativity is a good approximation. Nevertheless, since the height and bolometric luminosity of the lamps determine the temperature structure on the irradiated disc surface, and thus the UV/optical lag spectrum and SED, the Bowl model provides useful parameters for interpreting disc lags and SEDs from reverberation mapping experiments, especially if AGN accretion discs are flared and dusty like protoplanetary discs (Landt 2023).

A Bowl model fit is presented in Fig. 12, where Panel (a) shows the fit to the faint and bright disc SEDs, Panel (b) shows the fit to the interband lags, Panel (c) shows the temperature–radius profile, and Panel (d) shows the disc geometry. We employ MCMC methods to explore the parameter space, fitting typically 6-10 Bowl parameters with 26 constraints from the observed disc SEDs at minimum and maximum light, and 13 inter-band lags. In fitting the Bowl model to NGC 7469, we hold several parameters fixed. We adopt $M_{\bullet} = 9 \times 10^6 \text{ M}_{\odot}$ for the black hole mass (Bentz & Katz 2015). The luminosity distance $D_{\rm L} = 70.5$ Mpc is from the redshift. Given that broad emission lines are present in the spectrum, we may expect $i < 60^{\circ}$, but the disc inclination is not well determined. There is a strong degeneracy because the disc SED scales as $(M_{\bullet} \dot{M})^{2/3} \cos i$. After running a variety of fits with different parameter values free and fixed, we opt to present in Fig. 12 the fit for $i = 15^{\circ}$, matching the SED-fit results in Fig 11. Fig 12 presents the fit for $R_{\rm in} = 6 R_{\rm g}$ fixed at the ISCO radius of a spin-0 Schwarzshild black hole, and with the lamp height fixed at $H_r = 10 R_g$, which resolves its degeneracy with the change in irradiating luminosity ΔL_x , since the flat disc irradiation scales approximately as $H_x \Delta L_x$. Finally, we fix the H(r) power-law index $\beta = 100$, which produces a flat disc with a steep outer rim.

As discussed in Starkey et al. (2023), the Bowl model parameters can be optimized in three stages as follows. First, starting with a flat disc model (zero thickness), adjust \dot{M} and $R_{\rm in}$ to fit the faint disc SED. Turning up the lamp irradiation then increases the flat disc temperature by ΔT to match the change between the faint and bright disc SED. Such models fit the SEDs but underpredict the lags. Finally, adjust the size and shape of the disc H(R) profile to fit the lags. These adjustments can be done by hand to find rough initial parameter estimates that are subsequently refined by the MCMC algorithm. However, the burn-in stage of the MCMC algorithm succeeds in discovering the same result even when starting from very distant parameter values.

The faint disc T(R) profile (red curve in Fig. 12c) requires the blackbody emission from both sides of the disc to balance heating by viscous dissipation and torques associated with the accretion rate \dot{M} , thus using only the first term in equation (4). The fit parameters at this stage are \dot{M} and $R_{\rm in}$. Adjusting \dot{M} scales the $F_{\nu} \propto \nu^{1/3}$ segment of the flat-disc SED model to match the faint-disc SED data. This fit defines a lower limit, $\dot{M} < 0.0134~{\rm M}_{\odot}~{\rm yr}^{-1}$ because of course some irradiation elevates disc temperatures even at the minimum flux level.

The Bowl model places $R_{\rm in}$ at the ISCO radius, and thus $1 < R_{\rm in}/R_g < 9$, depending on the black hole spin. With \dot{M} constrained as noted above, increasing $R_{\rm in}$ lowers the maximum temperature and thus the UV end of the SED. The MCMC samples confirm the expected positive correlation between $R_{\rm in}$ and \dot{M} that keeps $T_{\rm max} > 2 \times 10^5$ K. The disc luminosity is $L_{\rm disc} = \eta \, \dot{M} \, c^2$, and with a radiative efficiency $\eta = \left(R_g/2 \, R_{\rm in} \right) = 1/12$ the faint disc model has an Eddington ratio $L/L_{\rm Edd} \sim 6$ per cent.

The maximum temperature needs to exceed $T_{\rm max} > 2 \times 10^5$ K to avoid a significant decrease on the UV end of the model SED. Turning

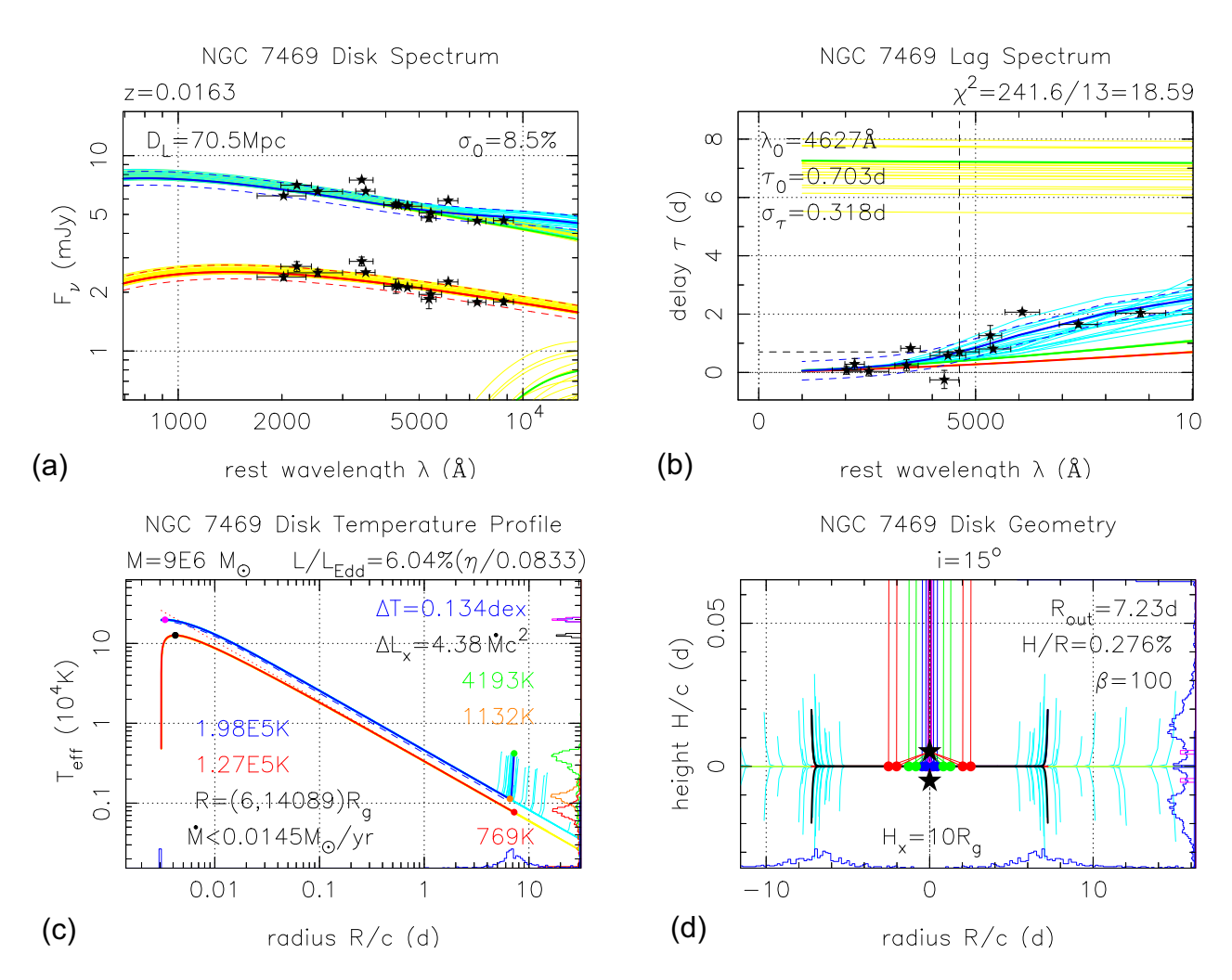


Figure 12. Bowl model fits to the disc SED and inter-band lag data for NGC 7469. The faint and bright disc SED data (a) and the inter-band lags (b) are compared with a blackbody reprocessing model for a thin disc, with a bowl-shaped power-law $H(R) \propto R^{\beta}$ profile, irradiated by a lamp post just above the black hole. The disc geometry (d) has a flat disc with a steep rim at $R_{\text{out}} \sim 5 - 10$ light d. The temperature profile (c) decreases as $T \propto R^{-3/4}$ on the flat disc, reaching a minimum and then rising to $\sim 4000 \, \text{K}$ on the inward-tilted face of the steep rim. With the lamp off (red curves) the model fits the faint-disc SED by adjusting the accretion rate \dot{M} to fit the red end and the inner radius R_{in} , hence maximum temperature, to fit the UV end. With the lamp on (blue curves), the disc temperatures rise and the SED flux increases to match the bright disc SED. In the upper panels, green curves show the bright state model SED and lag for the flat disc inside and the steep rim outside the temperature minimum. Time lags are dominated by the flat disc in the UV and are pulled toward the steep rim's lag in the optical. This transition from disc to rim reprocessing increases the optical lags to fit the lag data. Yellow and cyan curves show 30 random MCMC samples to indicate uncertainties in the constrained Bowl model. In the lower panels, histograms on the lower and right edges give uncertainties in fiducial temperatures, radii, and heights. Best-fitting parameters are collected in Table 6.

up by ΔL_x the bolometric luminosity of the lamp-posts above and below the disc plane, the additional irradiation increases the disc temperature profile, as shown by comparing the blue and red curves in Fig. 12(c). The disc temperatures rise by $\Delta T \approx 0.134$ dex, a factor 1.36, and the model SED rises by a corresponding factor $1.36^{8/3} \approx 2.3$ to match the increase between the faint and bright disc SED data, as shown in Fig. 12(a). Increased irradiation may arise from changes in the lamp height H_x and/or changes in its luminosity ΔL_x . The MCMC samples confirm the expected degeneracy between H_x and L_x , with the product L_x H_x being tightly constrained by the required rise in temperature needed to match the observed rise in flux.

With Bowl parameters \dot{M} , $R_{\rm in}$, and ΔT constrained to match the faint and bright disc SED, the flat-disc model predicts time delays that increase by about 1 d between 10^3 and 10^4 Å, as indicated by the red curve in Fig. 12(b). In contrast, the observed lags rise by about 2 d, a significant discrepancy. The model lags increase if we consider

a concave bowl-shaped power-law thickness profile $H \propto R^{\beta}$. This adds three parameters, the outer disc radius $R_{\rm out}$, the aspect ratio H/R, and the power-law index β . Irradiation of the concave disc increases temperatures in the outer disc more than the inner disc. This helpfully increases the model lags but also increases the red end of the SED and can upset the fit to SED data. The MCMC chain discovers that both constraints can be met with a high value of β to produce a flat inner disc with a steep outer rim. The resulting geometry, shown in Fig. 12(d), has a thin flat inner disc encircled by a thicker flared outer rim. The data constrain the rim radius to the range $R_{\rm out} \approx 5-10$ light d, with steeper rims ($\beta > 100$) at larger radii. The rim is steep but not tall, H/R < 1 per cent. This allows irradiation to pass over the top of the rim to illuminate structures such as the BLR and dusty torus at larger radii.

In fitting the Bowl model simultaneously to the lag and SED data, we include a noise model parameter, the fractional uncertainty

Table 6. Parameters of the Bowl model shown in Fig. 12.

Parameter	Symbol	Value	Units
Redshift	z	0.016268	_
Luminosity distance	$D_{ m L}$	70.5	Mpc
Inclination	i	15°	deg
Black hole mass	M	9×10^{6}	${ m M}_{\odot}$
Accretion rate	\dot{M}	< 0.0134	$M_{\odot}yr^{-1}$
Inner radius	$R_{ m in}$	6	GM/c^2
Outer radius	$R_{ m out}$	7.23	light d
Rim height	$H_{ m out}$	0.0276	$R_{ m out}$
Rim shape	$\beta \equiv d \ln H/d \ln R$	100	-
Irradiation	ΔT	0.134	dex
Lamp height	$H_{\scriptscriptstyle X}$	10	GM/c^2
Lamp luminosity	$\Delta L_{\scriptscriptstyle X}$	4.38	$\dot{M} c^2$
Disc efficiency	$\eta = L_{\rm disc}/\dot{M} c^2$	0.083	_
Disc luminosity	$L_{\rm disc} = \eta \dot{M} c^2$	0.060	$L_{ m Edd}$
Max temperature	$T_{ m max}$	>2.0	10^5 K
Rim temperature	$T_{\min} \rightarrow T_{\min}$	$1.1 \rightarrow 4.2$	10^3 K
SED uncertainty	σ_0	8.5	per cent
Lag uncertainty	$\sigma_{ au}$	0.32	d

 σ_0 , added in quadrature with the individual flux uncertainties σ_i . The standard maximum likelihood criterion implements the trade-off between lowering χ^2 to fit the data and lowering σ_0 to decrease the model SED uncertainties. A relatively large σ_0 softens the SED constraints and allows the MCMC chain to attend primarily to fitting the lags. The MCMC chain then lowers σ_0 , strengthening the SED constraints, and settles around $\sigma_0 \sim 9$ per cent. A similar parameter σ_τ applies to the lags, and the best-fit is for $\sigma_\tau \sim 0.3$ d. These noise model parameters quantify model uncertainty, since blackbody reprocessing neglects wavelength-dependent opacities that can produce Balmer edge and H α features increasing the lag and flux in the u and r bands.

To show more clearly how the disc rim increases the time lags, Fig. 13 shows the delay maps $\Psi(\tau|\lambda)$ for the Bowl model of Fig. 12. At UV wavelengths (black, purple, blue) the delay maps, are dominated by reprocessing on the flat disc. They rise to a peak and then decline, giving mean delays (vertical lines) that scale as $\tau_0 (\lambda/\lambda_0)^{4/3}$. At optical wavelengths (green, red) a U-shaped feature appears at longer lags, due to response on the steep rim where irradiation elevates the temperature to ~ 3000 K, emitting optical but very little UV light. The time lag at radius R spans the range $\tau = (1 \pm \sin i) R/c$. The response peak at $\tau = (1 - \cos i) R/c$, from the near side of the rim, is diminished because the rim here is tilted away from the observer, and vice versa for the peak at $\tau = (1 + \cos i) R/c$ from the far side tilted toward the observer. Thus the mean lag for the disc + rim geometry is a λ -dependent mix interpolating between small lags that scale as $\lambda^{4/3}$ in the UV, and larger lags from the steep rim, which dominates at longer optical and near infrared wavelengths.

Why should the disc have a steep rim at this radius? Note in Fig. 12(c) that the Bowl model's faint disc $T \propto R^{-3/4}$ profile (red) drops to ~ 1000 K at the rim, and the irradiated disc (blue) drops to a minimum temperature before rising to ~ 3000 K. The 1000–1500 K temperature range correspond to expected dust sublimation temperatures in the disc atmosphere. A similar rim temperature was found for a Bowl model fit to lag and SED data on NGC 5548 (Starkey et al. 2023) and Mrk 817 (Cackett et al. 2023). An increase in the disc thickness is expected outside this radius due to radiation pressure on dust grains in the disc atmosphere. Our findings are compatible with and lend support to the FRADO (Failed Radiatively Accelerated

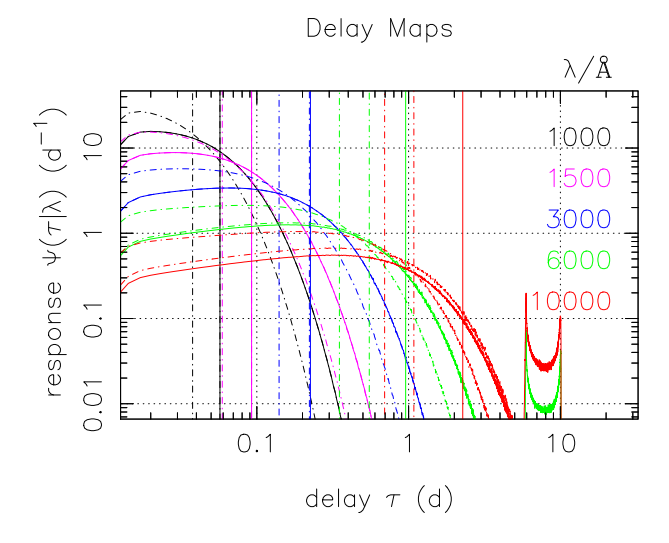


Figure 13. Delay maps $\Psi(\tau|\lambda)$, showing the time delay distribution of the response to changes in lamp-post luminosity, for the Bowl model in Fig. 12. The delay maps are plotted on a log-log scale for five wavelengths indicated by colours. The solid and dot–dash curves give the marginal response for the faint and bright states (red and blue curves in Fig. 12), respectively. At UV wavelengths (black, purple, blue) the response is dominated by reprocessing on the flat disc. These UV delay maps rise to a peak and then decline, giving mean delays (vertical lines) scaling as τ_0 $(\lambda/\lambda_0)^{4/3}$. At optical wavelengths (6000 and 10000) a U-shaped feature appears due to reprocessing on the steep rim, spanning the range $\tau = (1 \pm \sin i) R_{\rm out}/c$. The steep rim faces away from the observer on the near side, and is thus more visible on the far side of the inclined disc, significantly increasing the optical lags.

Dusty Outflow) wind model for the inner edge of the broad emissionline region (Czerny & Hryniewicz 2011). In this context, the disc rim is the base of the dusty outflow at the inner edge of the low-ionization BLR and should occur at the same temperature in all AGN.

Finally, note in Fig. 12(a) that the SED data are above the model in the u and r bands near 3600 and 6500 Å, respectively. Similarly, in Fig. 12(b), the lag data are above the model in both u and r. These lag and SED excesses are not straightforward to produce in a blackbody reprocessing model and may be interpreted as contributions of 10–20 per cent from the Balmer continuum in the u band and $H\alpha$ emission in the r band. Increased lags in the u band are seen in most if not all cases when intensive monitoring has succeeded in measuring reliable inter-band continuum lags. In the Bowl model, these increased lags and fluxes associated with Balmer emission may arise naturally if the steep rim encircling the disc has a region of optically thin gas near its crest, rather than the current model's sharp upper edge. An opacity-dependent rim height, taller at high-opacity wavelengths, should produce bound-free edges and emission-line features in the SED and lag spectra. The Bowl model might be elaborated to include these effects, but that is beyond the scope of this paper.

5.4 Diffuse continuum emission

The observed inter-band time lags, typically larger by a factor of 2 to 4 compared to theoretically predicted values, can arise in several ways. An important clue is the excess lag seen in the u band in many sources, and now also in the r band in our study of NGC 7469. These excess lags suggest that small time lags from the relatively compact accretion disc are increased by reverberations in the diffuse continuum and line emissions from the larger broad-line region (Lawther et al. 2018; Chelouche, Pozo Nuñez & Kaspi 2019; Korista

658

& Goad 2019). Netzer (2021) argues that the observed lags could be dominated by the BLR reverberations, diluted by flux from a compact zero-lag disc. An important point is that the u-band excess indicates that there is a Balmer continuum. However, the Balmer continuum lags should be at all wavelengths, not just the u band. So, simply ignoring the u band does not fully take into account the Balmer continuum lags and parameters determined from fitting lag versus lambda will not be correct.

Competing models currently ignore the BLR contribution but seek to increase the lags by modifying the standard thin-disc blackbody reverberations. In the relativistic disc + corona model, the lags are increased by elevating the height of the irradiating source, i.e. the corona, to several tens of R_g , by realistic treatment of X-ray reflections from the disc atmosphere, and by modifying the thermal emission from the irradiated disc by elevating the colour temperature by a factor $f_{\rm col} = 2.4$ above the effective temperature (Kammoun et al. 2019, 2021).

Simulations by Jaiswal et al. (2023) consider both the height of the irradiating source and the contribution from the diffuse continuum emission from the BLR. They find a degeneracy with both contributions being able to explain the observed lag spectra. However, they noticed also that for high accretion rate sources, this degeneracy could be resolved. This kind of modelling will be important to apply to real data to examine the exact contribution of diffuse BLR continuum and containing the corona height. It is also important to note that in their modelling the diffuse BLR contribution comes from the simple Thomson scattering but in reality, a more rigorous treatment of the photoionization physics, e.g. using CLOUDY, would be important.

6 SUMMARY AND CONCLUSIONS

We report the results of an intensive reverberation mapping campaign targeting NGC 7469, a Seyfert I galaxy with a circumnuclear starburst ring (Fig. 1). We used the LCO robotic telescope network to monitor variations in seven optical bands with sub-day cadence over 257 d (Fig. 2). Parallel monitoring at weekly intervals with *Swift* sampled variations in hard and soft X-rays and in three UV and three optical bands (Fig. 3).

We model the light curves, using the PYROA methodology, to derive inter-band time lags for 13 UV and optical bands (Fig. 5) and to decompose the observed variations into the constant SED of the host galaxy starlight and the variable SED from the AGN accretion disc (Fig. 6). The variable SED is close to a standard $F_{\nu} \propto \nu^{1/3}$ disc spectrum and maintains this SED shape while varying over a factor of 2.6 between the faintest and brightest states seen in the campaign. The lags collected in Table 1 and SEDs in Table 2 can be used to test models of reverberating accretion discs.

We fit the broad X-ray, UV, and optical SED with the KYNSED model in XSPEC to test and infer parameters of a relativistic disc + corona model in the Kerr geometry, treating the X-ray corona as an isotropic point source emitting a power-law X-ray spectrum powered from the inner disc and partially reflected from the irradiated accretion disc. The resulting SED fit achieved by MCMC methods is similar for black hole spin 0 and spin 1 (Fig. 7), with corresponding parameters (Table 3) including the inclination (65 or 41 deg), the accretion rate (16 or 13 per cent in Eddington units), corona height (25 or 41 R_g), and coronal power (75 or 90 per cent of the accretion power) transferred from the inner disc to the corona.

As in many previously studied cases, we find that the inter-band lags in NGC 7469 are consistent with $\tau \propto \lambda^{4/3}$, as predicted for a geometrically thin optically thick steady-state accretion disc with

 $T \propto R^{-3/4}$, but with lags that are up to 3 times larger than expected (Fig. 8). This suggests that the disc is larger at each wavelength and thus hotter at each radius than predicted.

We combined the SED and lag fits together to achieve the best-fitting values for the corona height and the accretion rate. Both the fits were explored for the grid of $f_{\rm col}$, and a plot summarizing fits is shown in Fig. 11. Based on the χ^2 distribution, we found that the best-fitting value for the $f_{\rm col}$ is 1.8, which seems to be quite high. We note that the irradiation model generates larger disc lags primarily by assuming that at every radius the disc colour temperature is a factor $f_{\rm col}=1.8$ larger than the effective temperature. This $f_{\rm col}$ parameter shifts the reverberation response at each radius to shorter wavelengths and lowers the surface brightness to maintain the effective temperature. That is plausible for the hot inner disc where electron scattering opacity dominates, but not for the lower temperature at which the optical emission is produced. As such $f_{\rm col}=1.8$ merely quantifies the problem of discs being hotter than expected in the standard model of blackbody reprocessing with $f_{\rm col}=1$.

We also consider a Bowl model (Starkey et al. 2023) that assumes blackbody reprocessing ($f_{\rm col}=1$) on a disc with a power-law thickness profile $H \propto R^{\beta}$. This Bowl model matches both the SED and lag constraints (Fig. 12) provided β is large enough to produce a flat inner disc geometry that determines the UV-optical SED and the UV lags, encircled by a steep rim that increases the optical lags. The fitted model places the rim near the radius where the disc temperature is similar to dust sublimation temperatures. This result supports models that invoke dust opacity to thicken the disc (Baskin & Laor 2018) and/or to launch a failed radiatively accelerated dusty outflow (FRADO) outside this radius (Czerny & Hryniewicz 2011), as is proposed to occur at the inner edge of the low-ionization BLR.

We note that the observed lags and SED fluxes are larger in the u and r bands relative to the adjacent bands and relative to the fitted models discussed above. The SED excesses imply a 10–20 per cent contribution of Balmer continuum emission in the u band and $H\alpha$ emission in the r band. However, rigorous modelling of the Balmer continuum at all wavelengths is required for a fair conclusion. The lag and SED constraints reported in our paper can now be used to test more detailed models that combine reverberations from the compact accretion disc and from the larger photoionized broad emission-line region, to assess the impact on the inferred parameters.

Finally, we note that monitoring of NGC 7469 is continuing with ground-based robotic telescopes in parallel with a more intensive sub-day cadence monitoring with *Swift* and *NICER* for analysis in future work.

ACKNOWLEDGEMENTS

We thank the anonymous referee for the constructive suggestions. This work makes use of observations from the Las Cumbres Observatory global telescope network. We acknowledge the use of public data from the *Swift* data archive. R. Prince is grateful for a visiting fellowship funded by the Scottish Universities Physics Alliance (SUPA). The project is partially supported by the Polish Funding Agency National Science Centre, project 2017/26/A/ST9/-00756 (MAESTRO 9) and the European Research Council (ERC) under the European Union's Horizon 2020 research and innovation program (grant agreement No. 951549) and BHU IoE scheme. HL acknowledges a Daphne Jackson Fellowship sponsored by the Science and Technology Facilities Council (STFC), UK. We also thank Tingting Liu and Marcin Marculewicz for their helpful comments.

DATA AVAILABILITY

The raw data sets were derived from sources in the public domain: LCO archive https://archive.lco.global and Swift archive https: //www.swift.ac.uk/swift_live. The inter-calibrated light curves are available on request. This research made extensive use of ASTROPY, a community-developed core PYTHON package for Astronomy (Astropy Collaboration 2013), MATPLOTLIB (Hunter 2007), and CORNER to visualize MCMC posterior distributions (Foreman-Mackey 2016).

```
REFERENCES
Armus L. et al., 2023, ApJ, 942, L37
Arnaud K. A., 1996, in Jacoby G. H., Barnes J., eds, ASP Conf. Ser.
   Vol. 101, Astronomical Data Analysis Software and Systems V. Astron.
   Soc. Pac., San Francisco, p. 17
Astropy Collaboration, 2013, A&A, 558, A33
Baskin A., Laor A., 2018, MNRAS, 474, 1970
Baumgartner W. H., Tueller J., Markwardt C. B., Skinner G. K., Barthelmy
   S., Mushotzky R. F., Evans P. A., Gehrels N., 2013, ApJS, 207, 19
Bentz M. C., Katz S., 2015, PASP, 127, 67
Bertin E., Arnouts S., 1996, A&AS, 117, 393
Blandford R. D., McKee C. F., 1982, ApJ, 255, 419
Brown T. M. et al., 2013, PASP, 125, 1031
Burrows D. N. et al., 2005, Space Sci. Rev., 120, 165
Cackett E. M., Horne K., Winkler H., 2007, MNRAS, 380, 669
Cackett E. M., Chiang C.-Y., McHardy I., Edelson R., Goad M. R., Horne K.,
   Korista K. T., 2018, ApJ, 857, 53
Cackett E. M. et al., 2020, ApJ, 896, 1
Cackett E. M. et al., 2023, ApJ, 958, 195
Chelouche D., Pozo Nuñez F., Kaspi S., 2019, Nat. Astron., 3, 251
Collier S. J. et al., 1998, ApJ, 500, 162
Combes F., 2023, preprint (arXiv:2302.12917)
Czerny B., Hryniewicz K., 2011, A&A, 525, L8
```

Díaz-Santos T., Alonso-Herrero A., Colina L., Ryder S. D., Knapen J. H., 2007, ApJ, 661, 149 Done C., Davis S. W., Jin C., Blaes O., Ward M., 2012, MNRAS, 420, 1848

Donnan F. R., Horne K., Hernández Santisteban J. V., 2021, MNRAS, 508,

Donnan F. R. et al., 2023, MNRAS, 523, 545

Dovčiak M., Papadakis I. E., Kammoun E. S., Zhang W., 2022, A&A, 661, A135

Edelson R. et al., 2015, ApJ, 806, 129

Edelson R. et al., 2017, ApJ, 840, 41

Edelson R. et al., 2019, ApJ, 870, 123

Evans P. A. et al., 2009, MNRAS, 397, 1177

Event Horizon Telescope Collaboration, 2019, ApJ, 875, L1

Event Horizon Telescope Collaboration, 2022, ApJ, 930, L12

Fathi K. et al., 2015, ApJ, 806, L34

Fausnaugh M. M. et al., 2016, ApJ, 821, 56

Fausnaugh M. M. et al., 2018, ApJ, 854, 107

Flewelling H. A. et al., 2020, ApJS, 251, 7

Foreman-Mackey D., 2016, J. Open Source Softw., 1, 24

Foreman-Mackey D., Hogg D. W., Lang D., Goodman J., 2013, PASP, 125,

Gardner E., Done C., 2017, MNRAS, 470, 3591

Gaskell C. M., 2017, MNRAS, 467, 226

Gehrels N. et al., 2004, ApJ, 611, 1005

Guo H., Barth A. J., Wang S., 2022, ApJ, 940, 20

Haardt F., Maraschi L., 1991, ApJ, 380, L51

Henden A. A., Levine S., Terrell D., Welch D. L., Munari U., Kloppenborg B. K., 2018, in AAS Meeting Abstracts #232. p. 223.06

Hernández Santisteban J. V. et al., 2020, MNRAS, 498, 5399

Hunter J. D., 2007, Comput. Sci. Eng., 9, 90

Jaiswal V. K., Prince R., Panda S., Czerny B., 2023, A&A, 670, A147

Kammoun E. S., Papadakis I. E., Dovčiak M., 2019, ApJ, 879, L24

Kammoun E. S., Papadakis I. E., Dovčiak M., 2021, MNRAS, 503, 4163

```
Kammoun E. S., Robin L., Papadakis I. E., Dovčiak M., Panagiotou C., 2023,
   MNRAS, 526, 138
```

Korista K. T., Goad M. R., 2001, ApJ, 553, 695

Korista K. T., Goad M. R., 2019, MNRAS, 489, 5284

Kormendy J., Ho L. C., 2013, ARA&A, 51, 511

Kubota A., Done C., 2018, MNRAS, 480, 1247

Kumari K. et al., 2023, MNRAS, 521, 4109

Landt H., 2023, Front. Astron. Space Sci., 10, 1256088

Lawther D., Goad M. R., Korista K. T., Ulrich O., Vestergaard M., 2018, MNRAS, 481, 533

Mahmoud R. D., Done C., 2020, MNRAS, 491, 5126

McHardy I. M. et al., 2014, MNRAS, 444, 1469

McHardy I. M. et al., 2018, MNRAS, 480, 2881

Mehdipour M. et al., 2018, A&A, 615, A72

Mirzaev T., Bambi C., Abdikamalov A. B., Jiang J., Liu H., Riaz S., Shashank S., 2024, ApJ, 976, 229

Nandra K., Clavel J., Edelson R. A., George I. M., Malkan M. A., Mushotzky R. F., Peterson B. M., Turner T. J., 1998, ApJ, 505, 594

Netzer H., 2021, MNRAS, 509, 2637

Netzer H., 2022, MNRAS, 509, 2637

Pahari M., McHardy I. M., Vincentelli F., Cackett E., Peterson B. M., Goad M., Gültekin K., Horne K., 2020, MNRAS, 494, 4057

Pal M., Naik S., 2018, MNRAS, 474, 5351

Peterson B. M., 2014, Space Sci. Rev., 183, 253

Peterson B. M. et al., 2004, ApJ, 613, 682

Roming P. W. A. et al., 2005, Space Sci. Rev., 120, 95

Schlegel D. J., Finkbeiner D. P., Davis M., 1998, ApJ, 500, 525

Seyfert C. K., 1943, ApJ, 97, 28

Shakura N. I., Sunyaev R. A., 1973, A&A, 24, 337

Shappee B. J. et al., 2014, ApJ, 788, 48

Shen Y. et al., 2024, ApJS, 272, 26

Shimura T., Takahara F., 1995, ApJ, 445, 780

Springob C. M., Haynes M. P., Giovanelli R., Kent B. R., 2005, ApJS, 160,

Starkey D. A., Huang J., Horne K., Lin D. N. C., 2023, MNRAS, 519, 2754 Sun M., Grier C. J., Peterson B. M., 2018, Astrophysics Source Code Library, record ascl:1805.032

Sun M. et al., 2020, ApJ, 902, 7

Tie S. S., Kochanek C. S., 2017, MNRAS, 473, 80

Troyer J., Starkey D., Cackett E. M., Bentz M. C., Goad M. R., Horne K., Seals J. E., 2016, MNRAS, 456, 4040

Wanders I. et al., 1997, ApJS, 113, 69

White R. J., Peterson B. M., 1994, PASP, 106, 879

APPENDIX A: COMPARISON OF PYROA WITH PYCCF

In this appendix, we compare the PYROA lag measurements derived by fitting the multiband light curve data (Section 3) with lag measurements from the more traditional Interpolated Cross-Correlation Function (ICCF) methodology (White & Peterson 1994), as implemented in the PYCCF code (Sun, Grier & Peterson 2018). The reported lags were determined by measuring the centroid of the CCF for values where the correlation coefficient $R > 0.8 R_{\text{max}}$, where $R_{\rm max}$ is the maximum correlation coefficient. The lag uncertainties were determined by 10⁴ Monte Carlo simulations using the flux randomization/random subset selection (FR/RSS). The PYCCF and PYROA lags are listed in Table A1. Their probability distributions can be compared in Fig A1.

The PYCCF and PYROA lags are consistent within their uncertainty estimates for all bands. However, the PYROA uncertainties are significantly smaller than those derived from PYCCF. For this reason we opted to use PYROA lags rather than PYCCF lags in our analysis. There are several reasons to consider for this difference:

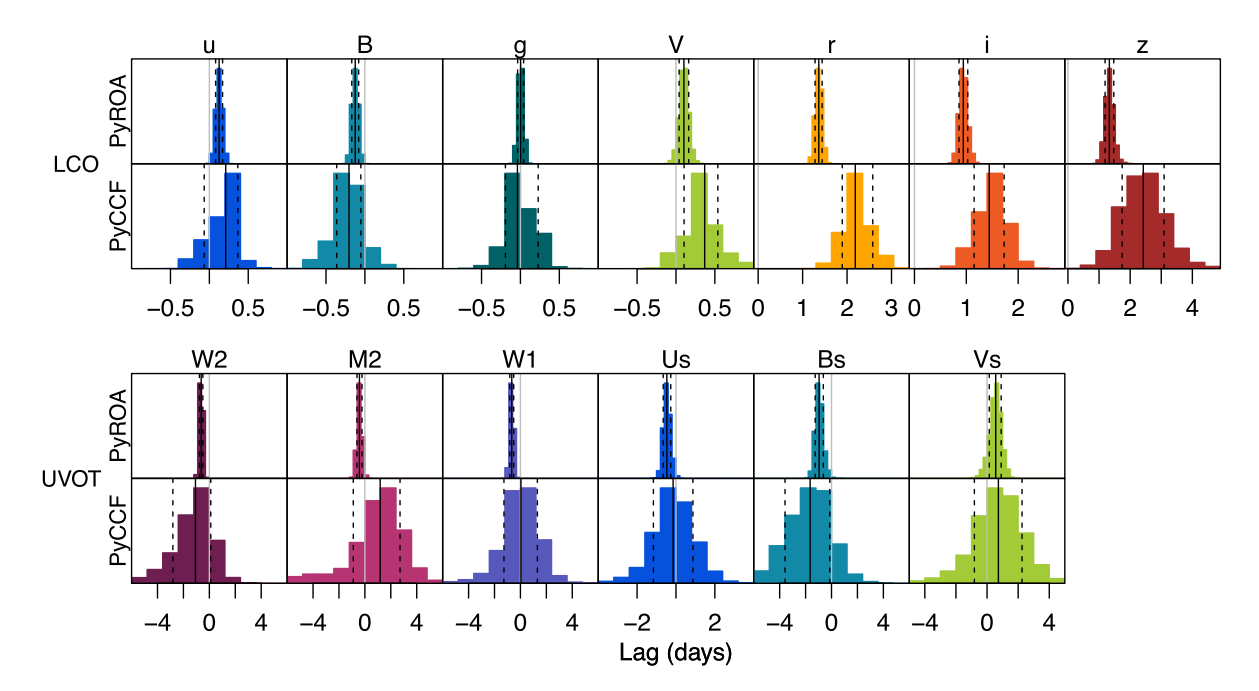


Figure A1. Comparison of derived lags from PYROA and ICCF method for LCO data (top panel) and for UVOT/Swift (bottom panel). The lags, 1σ uncertainties and the ratio between the uncertainties for each method are tabulated in Table A1.

Table A1. Comparison of lags derived from PYCCF and PYROA. Lag uncertainties from PYCCF are larger by factors of 3 to 5 than those from PYROA, consistent with what is derived in Donnan et al. (2021).

Bands	PYCCF	PYROA	$\sigma_{\mathrm{PYCCF}}/\sigma_{\mathrm{PYROA}}$
и	0.115 ± 0.148	0.082 ± -0.041	3.6
B	-0.204 ± 0.158	-0.156 ± -0.043	3.7
g	-0.039 ± 0.154	-0.039 ± -0.038	4.0
V	0.369 ± 0.265	0.044 ± -0.061	4.3
r	2.185 ± 0.293	1.266 ± -0.076	3.8
i	1.442 ± 0.292	0.844 ± -0.086	3.4
z	2.423 ± 0.679	1.223 ± -0.134	5.1

- (1) The FR/RSS method used to estimate ICCF lag uncertainties creates mock data sets using both bootstrap resampling (RSS = Random Subset Selection) and Monte-Carlo resampling of the measurement errors (FR = Flux Resampling). This standard procedure double-counts the statistical uncertainties. Tests with simulated light curve data (random walk plus Gaussian noise) indicate that this double-counting can increase the ICCF lag uncertainty estimates by a factor $\sqrt{2}$ for well-sampled data sets similar to these.
- (2) ICCF lag estimates give equal weight to each datum, rather than optimal inverse-variance weights used with the ROA and other light-curve fitting methods. We therefore expect smaller uncertainties for ROA lags. This makes little difference if the uncertainties are close to the same value, but could degrade ICCF lags if data with larger uncertainties are given undue weight.
- (3) The ROA light curve shape X(t) is defined by fitting all of the data. With many light curves defining X(t), it is effectively noise free (except in data gaps). ICCF linearly interpolates noisy data to define one or both light curves. Consequently, ICCF lags should be noisier by up to an additional factor of $\sqrt{2}$ (less if one light curve is much noisier than the other).
- (4) Noise in the reference light curve introduces a correlated error in the ICCF lags across all the echo light curves. Such correlations should be weaker for ROA lags where X(t) is effectively noise free.

This may be unimportant if the reference light curve is much higher S/N than the echo light curves.

- (5) The ROA model assumes that all light curves have the same shape, X(t), and thus a delta distribution for each of the interband lags. ICCF interpolates noisy data to define light curves with different shapes. As we expect a finite width and asymmetric delay distribution, with positive skew, the ROA lags should be shorter than the ICCF lags. Fig. A1 shows some evidence of this, particularly for the redder bands. However, large ICCF uncertainties tend to obscure this trend.
- (6) ROA lags from a fit that omits parameters for the width and shape of the delay distribution can be biased and their uncertainties can be underestimated, due to neglect of parameter covariances. This is important to consider when very good quality data provide information on higher moments of the delay distribution, such as significant smoothing or asymmetry of sharp light curve features at longer wavelengths. The PYROA fit residuals suggest that the delta distribution is not a bad approximation.
- (7) The ROA smoothing parameter Δ is a fit parameter optimized by minimizing the BIC. A more flexible X(t) introduces more parameters $p(\Delta)$. Rapid peaks and dips in the highest quality light curves may require a small Δ . When the delay distribution is asymmetric, with positive skew, the ROA lag has a positive correlation with Δ . The $\tau(\Delta)$ trend can be investigated to quantify and interpret this effect, but we have not pursued this here, since the simpler delta distribution model works well enough for our purposes.

¹Department of Physics, Institute of Science, Banaras Hindu University, Varanasi 221005, India

²Center for Theoretical Physics, Polish Academy of Sciences, Al.Lonikow, 32/46, 02-668 Warsaw, Poland

³SUPA School of Physics & Astronomy, University of St Andrews, North Haugh, St Andrews KY16 9NS, Scotland, UK

⁴Spectral Sciences Inc., 4 Fourth Ave., Burlington, MA 01803, USA

⁵Department of Physics and Astronomy, University of Southampton, Southampton, SO17 1BJ, UK

- ⁶Eureka Scientific Inc., 2452 Delmer St. Suite 100, Oakland, CA 94602, USA ⁷Research School of Astronomy & Astrophysics, The Australian National
- Research School of Astronomy & Astrophysics, The Australian National University, Canberra, ACT 2611, Australia
- ⁸Department of Physics, University of Oxford, Keble Road, Oxford OX1 3RH, UK
- ⁹Steward Observatory, University of Arizona, 933 North Cherry Avenue, Tucson, AZ 85721, USA
- ¹⁰DARK, The Niels Bohr Institute, University of Copenhagen, Jagtvej 155, DK-2200 Copenhagen N, Denmark
- ¹¹School of Physics and Astronomy and Wise Observatory, Tel Aviv University, Tel Aviv 6997801, Israel
- ¹²Department of Physics, University of Johannesburg, P.O.Box 524, 2006 Auckland Park, South Africa
- ¹³Department of Physics and Astronomy, Wayne State University, 666 W. Hancock Street, Detroit, MI 48201, USA
- ¹⁴Centre for Extragalactic Astronomy, Department of Physics, Durham University, South Road, Durham DH1 3LE, UK
- ¹⁵Department of Physics and Astronomy, 4129 Frederick Reines Hall, University of California, Irvine, CA 92697-4575, USA
- ¹⁶Department of Physics and Astronomy, University of California, Los Angeles, CA 90095, USA

- ¹⁷Department of Physics, University of California, 1 Shields Avenue, Davis, CA 95616-5270, USA
- ¹⁸Departamento de Astronom´ıa, Universidad de Chile, Casilla 36D, Santiago, Chile
- ¹⁹Department of Physics, Faculty of Natural Sciences, University of Haifa, Haifa 3498838, Israel
- ²⁰ Haifa Research Center for Theoretical Physics and Astrophysics, University of Haifa, Haifa 3498838, Israel
- ²¹South African Astronomical Observatory, P.O Box 9, Observatory Road, Observatory 7935, Cape Town, South Africa
- ²²School of Physics and Astronomy, University of Leicester, University Road, Leicester, LEI 7RH, UK
- ²³ Instituto de Astronomía, Universidad Nacional Autónoma de México, Km 103 Carretera Tijuana-Ensenada, 22860 Ensenada B.C., México
- ²⁴MIT Kavli Institute for Astrophysics and Space Research, Massachusetts Institute of Technology, Cambridge, MA 02139, USA
- ²⁵Department of Physics, University of Bath, Claverton Down, Bath BA2 7AY, UK

This paper has been typeset from a TEX/LATEX file prepared by the author.